Calibration of short-wave infraRed (SWIR) hyperspectral imaging using diffuse reflectance infrared Fourier transform spectroscopy (DRIFTS) to obtain continuous logging of mineral abundances along sediment cores

Stoil Chapkanski, Kevin Jacq, Gilles Brocard, Cécile Vittori, Maxime Debret, Andrea U De Giorgi, Daniele d'Ottavio, Enrico Maria Giuffré, Jean-Philippe Goiran

Calibration of Short-Wave InfraRed (SWIR) hyperspectral imaging using Diffuse Reflectance Infrared Fourier Transform spectroscopy (DRIFTS) to obtain continuous logging of mineral abundances along sediment cores

Chapkanski Stoil[1,2], Jacq Kévin[3], Brocard Gilles[1], Vittori Cécile[1,4], Debret Maxime[3], De Giorgi Andrea U., D'Ottavio Daniele[7], Giuffré Enrico Maria[8], Goiran Jean-Philippe[1]

[1]Archéorient, UMR 5133, University of Lyon 2-CNRS, 7 rue Raulin, 69007 Lyon, France.

[2]Laboratory of Physical Geography (LGP), UMR 8591, University Paris 1, Panthéon-Sorbonne – CNRS,1 place Aristide Briand, 92195 Paris, France.

[3]Normandie Univ, UNIROUEN, UNICAEN, CNRS, M2C, 76000 Rouen, France

[4]Laboratoire Image Ville Environnement (LIVE), UMR 7362, University of Strasbourg, Faculty of Geography and Urban planning, 3 rue de l'Argonne, 67083 Strasbourg, France

[5]Florida State University, Department of Classics, 324 Dodd Hall, Tallahassee, FL, 32306-1510, United States of America;

[6]Freie Universität, Insitut für Klassische Archäologie, Fabeckstraße 23-25, Berlin, 14195, Germany

[7]Unigeo S.r.l., Via Idrovore della Magliana, n. 147, Rome, Italia

[8]Soprintendenza Archeologia Belle Arti e Paesaggio per le Province di Siena, Grosseto e Arezzo, Siena, Italia

Corresponding author
Stoil Chapkanski
Laboratory of Physical Geography,
UMR 8591, Université Paris 1 Panthéon-Sorbonne - CNRS,
1 place Aristide Briand, 92195, Paris, France.
stoil.chapkanski@protonmail.com
+33 1 45 07 55 83

Abstract

Sediment cores are a major source of sub-surface data for a variety of environmental research endeavors, as well as mining and civil engineering applications. In paleo-environmental studies, fluctuations in mineral abundances along sediment cores are used to study climate change, sea-level variations, sediment dynamics, and landscape evolution. Increasing reliance on such proxies spurs the need for reliable and time-saving analytical tools and procedures. Diffuse Reflectance Infrared Fourier Transform spectroscopy (DRIFTS) is a rapid, non-destructive and accurate tool for quantification of mineral abundances. We use DRIFTS to calibrate Short-Wave InfraRed (SWIR) hyperspectral images (HSI) of a sediment core, in order to convert point-specific DRIFTS measurement of mineral abundances into a continuous record of mineral abundances along the core. Initially, single-phase and mineral assemblages of quartz, calcite, and clay mineral are created and measured by DRIFTS to establish calibration curves to convert DRIFTS data into mineral abundances, as $\%_{wt}$ of bulk sediment samples. Mineral abundances are then measured by DRIFTS in a set of 60 samples from a core drilled into the Albegna River delta, Tuscany, Italy in the Fall of 2020. SWIR-HSI of the core are then obtained and averaged over the areas corresponding to the samples taken for point-specific DRIFTS measurements. Least squares regressions are established between SWIR-HSI and DRIFTS data over these areas. This calibration is then used to convert SWIR-HSI of the entire core into a continuous prediction of quartz, calcite, and clay minerals abundances along the core. The continuous record highlights sharp changes in mineral composition, smeared out in the discontinuous DRIFTS record. The advantages and limitations of the method, as well as its applicability to other sedimentary environments are discussed.

Keywords: Infrared spectroscopy, hyperspectral imaging, sediment core, chemometrics, minerals, high resolution analysis

1. Introduction

Sediment cores are a major source of sub-surface information in stratigraphic and paleo-environmental studies. They are used to reconstruct past- climate (Miller et al., 2020), sea-levels (Kelsey et al., 2015), landscapes (Pennington et al., 2017) archeological environments (Delile et al., 2018; Salomon et al., 2018); for technical essays in mining and civil engineering (Kahraman et al., 2016), and for the assessment of natural (Grand Pre et al., 2012) and anthropogenic (Bigus et al., 2014) hazards. Variations of geochemical and mineralogical abundances along sediment cores are used as proxies for fluctuations of past climates (Solotchina et al., 2009; Wan et al., 2007; Tamburini et al., 2003), fluctuations in weathering rate, sedimentation rate, and shifts in depositional patterns (He et al., 2020; Wang et al., 2016; Hamdan et al., 2018; Lupker et al., 2012; Garzanti et al., 2010; 2011; Martinelli et al., 1993). They are used to assess sediment provenance and thereby track landscape evolution (Li et al., 2014; Andrews and Eberl, 2012; Liu et al., 2020; Pe-Piper et al., 2016; Heroy et al., 2003; Wahab and Stanley, 1991). Geochemical and mineralogical quantitative analyses traditionally resort to precise but time-consuming and expensive analytical methods, such as atomic absorption spectroscopy - AAS, inductive coupled plasma mass spectroscopy – ICP-MS (Willis, 1986), Scanning electron microscopy - SEM (Schulz et al., 2020), X-Ray diffraction - XRD (Moore and Robert, 1997) and Raman spectroscopy (Larkin, 2011). The accelerating growth of sediment core libraries worldwide has motivated the use of faster and less costly analytical approaches, such as portable X-ray fluorescence - PXRF (Duee et al., 2019), Attenuated Total Reflectance Fourier Transform Infrared spectroscopy - ATR-FTIRS (Milosevic, 2012), and Diffuse Reflectance Infrared Fourier Transform spectroscopy - DRIFTS (Frei and MacNeil, 2018). In the meantime, the need for high-resolution information on finely laminated sediments spurred the adaptation of non-destructive scanning and imaging techniques to sediment cores (Rothwell and Rack, 2006), most notably XRF core scanning (Davies et al., 2015), X-Ray tomography (Zonta et al., 2021; Paris et al., 2020), and hyperspectral imaging - HSI (Jacq et al., 2019a, b). Pioneering HSI on soils (Zaeem et al., 2021) and lake sediments (Makri et al., 2020; Rapuc et al., 2020; Ghanbari et al., 2020; Jacq et al., 2019a, b; Van Exem et al., 2018; Rivard et al., 2018; Butz et al., 2017; Aymerich et al., 2016) yields encouraging results. So far, HSI has been applied to organic-rich and silty-clayey lacustrine sediments and to nonwater-saturated sedimentary rocks with fairly homogenous grain size distribution

along core. The conversion of HSI data into chemical and mineral abundances requires calibration against standard analytical methods such as ICP-MS (Zaeem et al., 2021; Rivard et al., 2018), Loss on Ignition – LOI (Jacq et al., 2019b), particle size distribution – PSD (Jacq et al., 2019), and XRD (Greene et al., 2019).

FTIRS has been used for five decades (Srodo, 2002) to determine the abundance of carbonates (So et al., 2020; Henry et al., 2017), clay minerals (Srodo, 2002; Joussein et al., 2001), amorphous silica and quartz (Bertaux et al., 1998, Bandopadhyay, 2010; Melucci et al., 2019), other tectosilicates and sulfates (Muller et al., 2014; Bosch-Reig et al., 2017; Painter et al., 1978), total organic carbon (Vogel et al., 2008; Rosen et al., 2010; 2011; Hahn et al., 2011), metals (Moros et al., 2009; Siebielec et al., 2004), and plastic microparticles (Hahn et al., 2019).

We used DRIFTS to analyze the evolution of the provenance of sediments deposited during the Holocene in the delta of the Albegna River, in Tuscany, Italy, starting with a 14 m-long core obtained in 2020 (sediment core ALB-1). The analysis was conducted on samples, presenting an average separation of 20 cm. The analysis reveals that the sediment is almost exclusively composed of quartz, calcite and clay minerals, the abundances of which vary widely along core. In order to obtain a more continuous record of these variations, we use a high-resolution Short-Wave InfraRed (SWIR) hyperspectral images (HSI) of sediment core ALB-1, a core retrieved from the delta of the Albegna River, in Tuscany, Italy, in 2020. The HSI is averaged over the characteristic thickness (3 cm) of each of the DRIFTS samples. A calibration of the HSI data using the DRIFTS data is then conducted. It allows converting the HSI into a continuous record of mineral abundances at a resolution of 3 cm. Tectosilicates in general, and quartz in particular, are not detected by SWIR-HIS. In the case at hand, however, the simplicity of the mineral assemblage allows to adduce quartz abundance from the abundance of the two other dominant mineral groups. We also attempt to provide a site-specific prediction of quartz by expecting inverse correlations with calcite or by grain-size texture effects. Practically, the method involves first the establishment of calibration curves of mineral assemblages and DRIFTS data using synthetic mixtures of minerals, in order to convert DRIFTS data into quartz, calcite, and clay content. The calibration is applied to convert the DRIFTS signature of 60 samples from core ALB-1 into mineral abundances. The sediment displays marked variations in grain-size (from clay to pebble) and of moisture content along core. The SWIR-HSI of untreated core surfaces is not only sensitive to carbonates and clay minerals content, but also to grain-size and

120 moisture. We consider as work hypothesis that calibration of HSI data with DRIFTS of dry and
121 powdered samples could improve the continuous mineral logging along sediment cores. This
122 treatment reveals sharp step-chances in mineral abundances along the core that were poorly visible
123 in the discontinuous record, revealing the existence of very rapid (< 100 y), irreversible paleo-
124 environmental changes. After exposing these results, we discuss several aspects of the methodology.
125 We first discuss our selection of DRIFT spectra peaks to assess mineral abundances and the
126 replicability of this approach. We then discuss the relevance of the approach presented here to the
127 establishment of continuous records of mineral abundances in other geological settings. More
128 generally, we discuss the complementarity, advantages and limits of using a two infrared sensors
129 approach. Finally, we discuss the origin of the layering documented in core ALB-1 and the processes
130 that control it.

131 **2. General context**

132

133 Core ALB-1 was retrieved in 2020 from the Holocene fluvio-deltaic plain of the Albegna River, in
134 Tuscany, Italy (Fig.1). With a length of 70 km and a catchment area of 750 km², the Albegna River is
135 one of the main coastal rivers of Tuscany. The river originates near the Quaternary Monte Amiata
136 volcano, 1,738 m above sea-level (Fig. 1-A). The river flows south-westwards through Pliocene and
137 Quaternary basins (Cornamusini et al., 2011; Bossio et al., 2004). It reaches the Thyrrenian Sea north
138 of the Giannella sand spit (Fig.1-C). The tides along the Thyrrenian coast are microtidal averagely
139 ranging ~ 30 cm (Bertoni et al., 2020). The climate in the area is Mediterranean, with a mean annual
140 temperature of 13.8 °C along the coastal reaches and of 11°C in the Albegna headwaters. Mean
141 annual precipitation ranges from 700 mm/year at the coast to 1500 mm/year on Monte Amiata
142 (Marker et al., 2008). The Albegna River catchment drains Triassic-Cretaceous clayey calcareous
143 limestones, succeeded downstream by Oligocene sandstone, Miocene lagoonal and marine deposits
144 and finally Plio-Pleistocene marine clays close to the coast (Fig. 1-B, Cornamusini et al., 2011; Bossio
145 et al., 2004; Bertini et al., 1967). A sizeable volume of sediments derived from these formations
146 contributes to the > 30 m-thick Holocene infill of the Albegna lower valley, which was incised during
147 the last glacial marine low stands (Mazzini et al., 1999). Geochemical and mineralogical data from
148 widely scattered 30 surface silty-clay samples in the catchments of the Albegna and Fiora Rivers
149 (Gliozzo et al., 2014) indicate mineral abundances in the range of 15-70% for phyllosilicates, 9- 58%

for quartz, and 1-34% for calcite. Phyllosilicates consist mainly of kaolinite, illite, smectite and chlorite. Feldspars (2-6%), dolomite (0-3%) and hematite (0-1%) are detected but are much less abundant.

3. Material and Methods

3.1. Field drilling

Mechanical rotation coring was conducted on the left bank of the Albegna River, +1.5 m above the mean sea-level, close to the river mouth (Fig. 1C), next to the historic Forte delle Saline Renaissance fortified tower, and next to the Roman fluvial port of Albinia. The site lies 200 m south of the Albegna River channel, 500 m east of the sea, and 700 m north of the lagoon of Orbetello. An outer core liner was used to prevent contamination of core sections by core wall material during drilling operations. Coring allowed the retrieval of a 14 m-long continuous sedimentary succession. Stratigraphic description in the field includes estimates of sediment color, texture, hardness, and the presence of oxidation, shells, and plant fragments. Absolute ages were obtained by accelerator mass spectrometry radiocarbon dating. The samples were process in the Center for Radiocarbon dating of Lyon UMR 5138, and measured at the LMC14 Artemis Laboratory in Saclay, France (Table 1). Radiocarbon ages were converted into calendar years using the IntCal20 Northern Hemishpere atmospheric calibration curve (Reimer et al., 2020).

3.2. Methodological approach

The approach involves five consecutive steps (Fig.2). The part of the sediment core comprised between 2 m and 13.5 m below the ground surface was extracted continuously using a 2 cm-wide plastic U-channel. A total of 11.5 meters, split into 23 U-channel sub-sections (50 cm each) were entirely scanned by SWIR-HSI (Step 1). U-channels prevent damaging of laminated sequences during transport, especially highly non-cohesive sand layers. After image acquisitions, sixty samples were taken from the U-channels (see section 3.2.2.) and measured by DRIFTS (Step 2). Synthetic mineral mixtures were prepared to calibrate the conversion of these DRIFTS data into mineral abundances (Step 3). DRIFTS and SWIR-HSI data were then compared over the areas of DRIFTS sampling to convert SWIR-HSI data into mineral abundances (Step 4). This calibration was then used to obtain a 3 cm-resolution continuous record of mineral abundances along the core (Step 5).

180 3.2.1. **Hyperspectral imaging** (Step 1)

181 Short-Wave Infrared (SWIR, Specim Ltd., Finland, OLES22.5) hyperspectral imaging of the sediment
182 core was obtained following the protocol described in Jacq et al. (2020b). The resulting image is 1 cm
183 wide and 11.5 m long. It consists of 45 columns and 53,220 lines of 185 µm²-sized pixels. Each pixel
184 contains a record of 288 individual spectral channels spanning a range of 3,880-10,354 cm^{-1},
185 corresponding to a wavelength range of 965 to 2,576 nm, with a 5.6 nm resolution. The spectra were
186 subsampled between 3,966 and 9,781 cm^{-1} (1,016-2,526 nm) in order to remove noisy wavelengths.
187 Reflectance spectra were then converted into pseudo-absorbance values, and pretreated by Standard
188 Normal Variate and a baseline to be formatted in the same way as the DRIFTS data (Matlab R2020a,
189 Mathworks, USA). SWIR-HSI spectra are presented in wavelength (nm) units.
190

191 **3.2.2. Sediment core sampling (Step 2)**

192 Magnetic susceptibility logging of the core (Dearing, 1999) was conducted at 3 cm-resolution using a
193 Bartington MS2 susceptibilimeter and MS2F probe (Oxon, UK) in cgs units (centimeter-gram-second
194 system) before the sampling of the core. Samples 3cm-thick were collected every 20 cm for DRIFTS
195 (Figure 2, Step 2). Additional samples were collected in the thinnest stratigraphic units in order to
196 prevent under-sampling of these units. The samples were dried in an oven at 50°C for seven days.
197 The proportions of clay-silt, sand, and coarser fractions were measured by wet sieving through 0.063
198 mm and 2 mm-mesh size stainless steel sieves of 10 g of sediment. The sand fraction was sieved at
199 0.25, 0,5 and 1 mm to document grain-size distribution in the sand fraction (fine/medium/coarse
200 sand). Subsamples of 5 g bulk sediment were set aside before the sieving and manually grinded
201 using an agate mortar into a fine homogenous powder. The powder was dried at 50°C for 24h prior to
202 spectroscopic measurement.
203

204 **3.2.3. Reference minerals and synthetic mineral assemblages (Step 3-A)**

205 42 synthetic mineral assemblages were produced for the calibration of the DRIFTS data. Powders of
206 pure quartz (SiO2), calcite ($CaCO_3$), kaolinite ($Al_2Si_2O_5(OH)_4$), montmorillonite
207 ($(Na,Ca)_{0,3}(Al,Mg)_2Si_4O_{10}(OH)_2$) and illite ($K,H_3O(Al,Mg,Fe)_2(Si,Al)_4O_{10}[(OH)_2 \cdot (H_2O)]$) were used from
208 previously established mineral spectra databases (Chapkanski et al., 2021a,b). Samples (1 g each) of
209 pure minerals were prepared by mixing oven-dried spectroscopic-grade potassium bromide (KBr) with

quartz (Q) and calcite (Ca). The clay minerals (Cm) were represented by a 1:1:1 mixture of kaolinite, montmorillonite and illite. Clay species can be successfully discriminated by FTIR spectroscopy (Srodo, 2002; Joussein et al., 2001), but, because their specific absorption bands overlap, it was decided to only consider their spectral signature collectively, to avoid any confusion (Muller et al., 2014). Further combinations were prepared: Q + Ca, Q + Cm, Ca + Cm and Q + Ca + Cm (Table 2). Precision of ± 0.1 mg is required when weighing. The powders were mixed by hand using an agate mortar and pestle for five minutes, in dry conditions. The samples were finally stored in an oven for 12 hours prior to spectroscopic measurement to maintain a low moisture content.

3.2.4. DRIFTS analysis (Step 3-B)

Diffuse Reflectance Infrared Fourier Transform Spectroscopy (DRIFTS) was conducted on the sediment core samples and on the synthetic mixtures. The texture of the powders ensures a good and homogenous penetration of infrared light into the samples (Bertaux et al., 1998). The mid-reflected infrared light spectrum of each sample was obtained using a FT-IR Frontier Spectrometer with a KBr beam splitter, a diffuse reflectance sampling accessory and a TGS detector (PerkinElmer, Waltham, MA, USA). Spectroscopic measurements were conducted in a temperature- and humidity-controlled room to ensure stable and constant optical air properties during measurement. 10 mg of each sample was placed into a micro-cup and scanned from 4,000 to 450 cm^{-1}, with a 1 cm^{-1} resolution, corresponding to wavelengths of 2,500 to 22,222 nm. Dried powdered potassium bromide (KBr) was used as background sample. Supplementary technical details are provided in Chapkanski et al., (2020). Middle Infrared spectral data feed a data matrix of “n” lines (where “n” is the number of spectra/samples) and “p” columns (where “p” is the quantity of spectral bands). The reflectance spectra were converted to absorbance, standardized, and finely baselined using Standard Normal Variate and Baseline pretreatments (Camo Unscrambler 10.3, Oslo, Norway). DRIFT spectra are presented in wavenumber (cm^{-1}) units.

3.3. Conversion of DRIFT spectra into mineral abundances (Step 3-C)

Absorbance mid-infrared spectroscopy has been applied to the quantification of mineral assemblages (Srodon, 2002) because the amount of absorbed infrared radiation is proportional to the mineral mass fraction (%weight), thus obeying to the Lamber-Beer’s law (Pichard and Frohlich, 1986; Bertaux et al.,

1998). Therefore, simple linear regressions (Moosavi and Ghassabian, 2018) can be applied to convert the areas of absorbance peaks into weight concentrations (Table 2). Spectroscopic measurements were repeated three times on each synthetic mixture to assess reproducibility. The most discriminating absorbance peaks were selected to quantify the %weight of each mineral species. The center of these peaks are located as follows: for quartz (Q) at 1,874 cm^{-1}, 1,160 cm^{-1}, and 696 cm^{-1}; for calcite (Ca) at 2,512 cm^{-1}, 875 cm^{-1}, and 848 cm^{-1}; and for clay minerals (Cm) at 3,696 cm^{-1}, 3,622 cm^{-1}, and 1,112 cm^{-1}. The baselined area of these peaks was quantified using the software PerkinElmer Spectrum (Waltham, MA, USA). Overlapping peak areas between the discriminating peaks were excluded to avoid over-quantification. Pure mineral end-members were used as zero-abundance standards for other end-member minerals. For instance, the pure quartz spectrum was used as standard zero for calcite calibration. Therefore, the linear regression was used to provide Q, Ca and Cm mineral weight estimates for each sample following: Mineral weight % = (peak area - a)/b. Linear coefficient of determination (R^2), mean values, and the standard deviations of residual values were used to evaluate the performance of the calibration (Moosavi and Ghassabian, 2018). Best curve calibrations were obtained at 1,160 cm^{-1} for quartz, 2,512 cm^{-1} for calcite, and 3,622 cm^{-1} for clays. The calibration was then used to quantify mineral species in the synthetic assemblages in order to evaluate the performance of the calibration on samples of known composition (Table 2). Finally, the calibration was used for the quantification of Q, Ca, and Cm abundances in the 60 samples of core ALB-1.

3.4. Calibration of HSI data for mineral abundance prediction (Step 4 and 5)

The hyperspectral image was down-sampled to a 3 cm-core thickness resolution over the areas occupied by each DRIFTS sample, such as to match the DRIFTS measurements. The DRIFTS-derived mineral abundance of the 60 sampling depth intervals (Fig. 2) was then matched to the corresponding SWIR-HSI spectra matrices. The two datasets were then subjected to partial least squares regressions (Wold et al., 1984) using the software Camo Unscrambler 10.3 (Oslo, Norway) to relate quartz, calcite and clay mineral abundances to the corresponding SWIR-HSI spectra obtained by hyperspectral imaging. Linear coefficients of determination (R^2) and root mean square errors (RMSE) were used to evaluate the performance of these regressions and p-values were provided to verify their statistical significances. Regression coefficient weight vectors of cumulated PLSR

components were used to assess the contribution of each wavelength to the correlation. The calibration was then used to assess the abundance of quartz, calcite, and clay minerals continuously along core ALB-1 at 3 cm-resolution using the SWIR-HSI spectral dataset, yielding a total of 313 measurements over the 14 m-long core. The same PLSR model was also applied to produce maps of mineral abundances. The same PLSR model was also applied to all the HSI pixels (45 columns by 53,220 lines) to produce mineral abundance maps and characterize the deposits at resolution of 185 µm.

4. Results

4.1. Stratigraphy, grain-size and magnetic susceptibility in core ALB-1

Sediment core ALB-1 intersected three main stratigraphic units (Fig.3). Basal Unit 1 (- 13.5 to - 8.5 m depth) is relatively homogenous and is composed of up to 70‰$_{wt}$ fine- to medium-sized grey shelly sand. Its magnetic susceptibility (MS) is low (0-80 cgs). Shell concentration is highest at its base (sub-unit 1-A) while the overlying sub-unit 1-B shows coarser and homogenous sands. Unit 2 (- 8.5 to - 3.5 m depth) is extremely heterogeneous and composed of alternations of silty clays and sand layers. Brownish, poorly magnetic silty clays at the base of unit 2 (in SU2-A) amount to 70‰$_{wt}$ of the sediment. The overlaying sub-unit 2-B is a succession of grey clayey/shelly sand and gravel. Magnetic values range from 0 to 300 cgs with marked peaks in coarse sand and gravely layers. The topmost sub-unit (2-C) is made of interbedded brown, weathered silty clay and sand layers. A well-sorted brown medium sand (70‰$_{wt}$ of the sand fraction) layer marks the top of sub-unit 2C. Magnetic susceptibly decreases upward throughout unit 2. The last, and topmost stratigraphic unit (SU3) consists of massive, weathered grey silty clay (90‰$_{wt}$ of the sediment) dotted by carbonate concretions near its base (SU3-A). Its upper part (SU3-B) is made of dark brown alternations of silty clay and sand containing roman pottery sherds with MS values ranging from 0 to 200 cgs.

4.2. Peak identification of Infrared spectra

4.2.1. DRIFT spectra of synthetic assemblages

A selection of DRIFT spectra of pure mineral species and species combination is provided on Figure 4. Quartz exhibits distinctive absorbance peaks at 1,872 cm^{-1}, 1,610 cm^{-1}, 1,352 cm^{-1}, 1,160 cm^{-1}, 813 cm^{-1} and 696 cm^{-1}. Calcite is identified by peaks at 2,984 cm^{-1}, 2,874 cm^{-1}, 2,512 cm^{-1}, 1,797 cm^{-1},

299 1,623 cm^{-1}, 1,400 cm^{-1}, 875 cm^{-1}, 848 cm^{-1}, and 714 cm^{-1}. Clays (kaolinite, montmorillonite, and illite)
300 absorb mostly at 3,696 cm^{-1}, 3,624 cm^{-1}, 1,240 cm^{-1}, 1,111 cm^{-1} and 792 cm^{-1}.
301
302 **4.2.2. DRIFT spectra of core samples**
303 Figure 5 provides descriptive statistics (mean, maximum, minimum, Q1 and Q3 quartiles) of all
304 combined core sample DRIFT spectra in the SWIR and MIR light ranges. Absorbance peaks were
305 attributed to specific inorganic and organic compounds using previously established mineralogical
306 spectra database (Chapkanski et al., 2021a,b) as well as extensive spectra libraries (Chukanov and
307 Chervonnyi, 2016). Clay minerals, especially Kaolinite - $Al_2Si_2O_5(OH)_4$ and Montmorillonite -
308 $(Na,Ca)_{0,3}(Al,Mg)_2Si_4O_{10}(OH)_2$) are associated with absorbance peaks at 3,696 and 3,626 cm^{-1} and
309 around 3,400 to 3,350 cm^{-1} in the O - H stretching vibration region. Carbonates, especially calcite
310 $CaCO_3$ is associated with absorbance peaks at 2,986 cm^{-1}, 2,876 cm^{-1}, 2,640 to 2,460 cm^{-1}, 1,460 to
311 1,360 cm^{-1} and 874 cm^{-1}. Tectosilicates, especially quartz (SiO_2) clearly absorb at 1,160 and 696 cm^{-1}
312 while peak of feldspars occurs at 1,290 to 1,270 and 795 cm^{-1} and could be specifically attributed to
313 albite $NaAlSi_3O_8$ and orthoclase $KAlSi_3O_8$. Inosilicate and nesosilicate minerals could absorb at 970
314 and 650 cm^{-1}. Chlorite and mica groups generated the absorbance peak observed at 1,630 cm^{-1}.
315 Aliphatic C-H bands absorb at 2,930 cm^{-1} and unsaturated bands of alkenes C=C absorb at 1,642 cm^{-1}
316 .
317
318 **4.2.3. Short-Wave Infrared spectra of sediment core images**
319 The SWIR spectra show areas of absorbance related to organic and inorganic compounds (Fig. 5).
320 The two main absorption peaks near 1,440 nm and 1,925 nm are produced by hydroxyl bonds mainly
321 induced by moisture (Palmer and Williams, 1974), but they can also be produced by organic and
322 inorganic compounds, especially clays. Clays show absorption peaks related to Al-OH bonds between
323 2,200-2,220 nm and to O-H bonds around 1,410 nm, 2,340 nm and 2,450 nm (Madejova et al., 2017).
324 Carbonates, chlorite and micas also produce multiple absorption peaks around 2,282 and between
325 2,310-2340 nm, but these often overlap with other compounds, such as organic matter (Cloutis, 1989;
326 Krupnik and Khan, 2019; Viscarra Rossel and Behrens, 2010). Organic (C-H) bonds produce
327 numerous absorption peaks, especially around 1,056 nm, 1,146 nm, 1,400 nm, 2,300-2,350 nm and

2,400-2,450 nm (Cloutis, 1989). Tectosilicates, including quartz, have no specific absorption peaks in the investigated spectral range (Krupnik and Khan, 2019).

4.3. Calibrations of mineral abundances

4.3.1 Performance of the synthetic sample cross-calibration

Weight concentrations (wt%) of minerals (quartz, calcite and clay minerals) were obtained using linear regression equations (Fig 6). Predicted values were plotted against known weight concentrations in order to evaluate the performance of the mineral quantifications (Fig. 6). Quartz, calcite and clay minerals were successfully predicted in single and multi-phase samples with R^2 > of 0.9. All correlations are significant with p-values < 0.05. Mean and standard deviations of residual values show slight underestimation of the prediction in single and multi-phases (from -0.5 to -1.5). The standard deviation ranges from 2.2 to 7.

4.3.2 Performance of the synthetic sample to core sample DRIFTS calibration

The linear regressions established using our synthetic standards were applied to the mid- infrared spectrum of the sediment cores samples (total of 60) to calculate quartz, calcite and clay minerals abundances (Fig. 3.C). Predicted values (in wt%) range between 14 and 64% (±0.2) for quartz, 0 and 43% (±0.7) for calcite, and 0 and 41% (±0.9) for clays. Quartz wt% is positively correlated with medium (0.48) and fine (0.53) sand fractions and bears negative correlation with the silty-clay (-0.56) fraction (Table 3). In contrast, clay minerals wt% is highly correlated to the clay-silt fraction (0.91) and negatively correlated to the medium (-0.78) and fine (-0.52) sand fractions. Calcite wt% shows no specific correlation with any grain-size fraction.

4.4 Calculation of mineral abundance along core ALB-1

4.4.1 Performance of the DRIFTS-core SWIR image calibration

Partial least squares regression (PLSR) was used to create a predictive model of quartz, calcite and clay abundance at regularly spaced, 3 cm-thick intervals along core ALB-1. The PLSR calibration was carried out between DRIFTS-derived mineral abundances in the 60 core samples and their SWIR spectra obtained by hyperspectral imaging (see section 3.4). The PLSR statistical performance is shown on Fig. 7. Quartz wt%, calcite wt%, and clay minerals wt% are successfully predicted based on

358 the SWIR spectra using seven latent variables (PLS components). In addition to statistical
359 parameters, the plot analysis of the raw regression coefficients allows for evaluating the influence of
360 absorbance bands on the PLS regression loading weights (Vogel et al., 2008; Hahn et al., 2011;
361 2018). High coefficients (either positive or negative) contribute significantly to the prediction of the
362 major mineralogical components (Fig. 7). Calcite regression coefficients show positive values for
363 spectral regions specific to carbonates (2,237 nm, 2,500 nm) and organic matter (1,056 nm, 1,146
364 nm), and negative values for spectral regions induced by clays (1,422 nm, 2,208 nm and 2,415 nm,
365 Cloutis, 1989; Krupnik and Khan, 2019; Madejova et al., 2018; Viscarra Rossel and Behrens, 2010).
366 Positive regression coefficients of clay minerals are related to specific wavelengths of phyllosilicates
367 (1,411 nm, 1,900 nm, 2,202 nm and between 2,380-2,450 nm), while the negative coefficients are
368 related to hydroxyl bonds probably induced by interstitial moisture between the coarser grains (1,445
369 nm, 1,838 nm, 1,945 nm) and to chlorites (2,292 nm, Palmer and Williams, 1974; Cloutis, 1989;
370 Krupnik and Khan, 2019; Viscarra Rossel and Behrens, 2010). Quartz regression coefficients show
371 positive values for spectral regions specific to hydroxyl bonds (1,445 nm and 1,945 nm) and stand out
372 for their anti-correlation with carbonates (-0.82) and clay minerals (-0.42), particularly pronounced for
373 the hydroxyl and carbonates bonds (2,237 nm, 2,500 nm, Fig. 7).
374
375 **4.4.2. Performance of the continuous logging and mineral mapping along core ALB-1**
376 The calibrated PLSR model was applied to each hyperspectral image data averaged over 3 cm bins,
377 along the sediment (total of 313 bins) in order to assign continuous logging mineral abundances of
378 quartz, calcite and clay minerals (Fig. 3.D). Predicted values range within 19-58% (±4) for quartz, 4-
379 48% (±3) for calcite and 0-37% (±3) for clay minerals. They display a high degree of agreement with
380 DRIFTS-derived abundances. Predicted quartz wt% is positively correlated with fine-sand (0.62) and
381 total sand (0.60) fractions, and shows negative correlations with clay minerals (-0.68) and the clay-silt
382 fraction (-0.58, Table 3). Predicted calcite wt% shows no specific correlations with other mineralogical
383 or physical properties of sediments. Predicted clay minerals wt% show strong correlation with the
384 clay-silt fraction (0.86) and hydroxyl bonds peak at 1,450 nm (0.68) and are negatively correlated to
385 the total and medium sand fractions. The basal stratigraphic unit (SU1) is notably rich in quartz and
386 poor in clay compared to other units. For SU1, differences between SWIR-HSI predicted and DRIFTS
387 inferred mineral abundances are averagely 0.33, -0.44 and -0.27 for quartz, calcite and clays

388 respectively. The high resolution maps of mineral abundances (Fig.3D) reveal a faint layering
389 produced by fluctuations in quartz abundance, while calcite and clay content remains fairly stable.
390 The medium stratigraphic units (SU2) is highly heterogeneous, but it stands out for its higher calcite
391 content than units SU1 and SU3, and for its higher clay content relative to SU1. For SU2, differences
392 between predicted and observed mineral abundances are averagely -1.07, 0.26 and -0.35 for quartz,
393 calcite and clays. SU3 is notably clay-rich and calcite-poor compared to the other units. For this unit,
394 differences between predicted and observed mineral abundances are averagely 5.07, 0.17 and 1.34
395 for quartz, calcite and clays respectively.
396
397 **5. Discussion**
398 **5.1. Peak selection for DRIFTS assessment of mineral abundances and replicability**
399 Numerous studies reported satisfactory mineral calibrations and predictions using Fourier Transform
400 InfraRed (FTIR) measurements on samples with known mineral contents (Pichard and Frohlich, 1986;
401 Bertaux et al., 1998; Moosavi and Ghassabian, 2018). Based on these previous approaches, we
402 converted DRIFTS data into mineral abundances using linear regressions calibrated on single and
403 multi-phase synthetic mineral assemblages. Qualitatively, quartz, calcite and clay minerals can be
404 identified easily in the infrared spectra (Fig. 4) owing to their specific peaks. In quantitative
405 investigations, however, non-overlapping peaks should be selected (Pichard and Frohlich, 1986).
406 Previous quantitative studies used peaks centered at 693 cm^{-1} and 712 cm^{-1} to respectively assess
407 quartz and calcite abundances (Pichard and Frohlich, 1986). At these wavenumbers, however,
408 overlaps with clay mineral peaks tend to generate unwanted quantitative distortions, so that better
409 predictions were obtained using 1,160 cm^{-1} for quartz and 2,512 cm^{-1} for calcite. Calcite is the most
410 abundant carbonate mineral in our sedimentary sequence, but its peak could be produced in other
411 natural environments by additional carbonates, in particular aragonite (triple bond at 2,546, 2,524 and
412 2,500 cm^{-1}), dolomite (2,526 cm^{-1}) and magnesite (2,538 cm^{-1}). Among clay minerals, slight chemical
413 variations can induce overlapping bonds (Madejova and Komadel, 2001) and different peak shapes
414 (Henry et al., 2017). To overcome this problem, we have combined kaolinite, montmorillonite, and illite
415 absorbances (Muller et al., 2014). The best calibration was obtained using a peak centered at 3,622
416 cm^{-1}, where the three clay species absorb. The accuracy of the linear regressions (Fig. 6) is
417 satisfactory, with high R^2 coefficients, low residual values, and therefore a direct relationship between

absorbance and mineral abundance. Still, discrepancies between known single-phase mineral concentrations and DRIFTS-inferred abundances tend to increase at very low (< of 2%) and high (> of 50%) mineral concentration (Henry et al., 2017). Departure from the linear regression at high concentration could result from the lower density of the synthetic powder at such values, whereas departures at low concentration could be influenced by detection limits (Vogel et al., 2016). In multi-phase mineral concentrations, DRIFTS-inferred abundances remain satisfactory (Fig. 6) showing that the chosen peaks are not influenced by the absorbance of other minerals.

PLS regressions have been widely used to calibrate mineral abundances in FTIR spectra (Fernandes et al., 2020; Hahn et al., 2018; Muller et al., 2014). Predictions often show great performances and efficiency because the calibrations are based on the entire set of wavenumbers and therefore all absorbance peaks are considered. However, as certain peaks are common for two or more mineral phases, leading to over or under estimations (Vogel et al., 2016). Besides, the PLS calibration is population-specific, and must be rerun on each new dataset requiring the availability of the entire calibration dataset. However, these later are often inaccessible. To overcome this issue, this study provides linear regressions that are easily reusable for natural sediment spectra.

5.2. Calibration of high-resolution imaging SWIR spectra and DRIFTS-inferred mineral abundances

In the mid-infrared range used in DRIFTS, absorbance is controlled by vibrations of molecular bonds and functional groups. Therefore, peaks are very meaningful in the detection of carbonates and silicates (Fig. 5). By contrast, in the shorter infrared range (SWIR), absorbance is controlled by broad bonds, overtones and combination of functional groups (Robertson et al., 2016). Consequently, HSI-derived spectra are not sensitive to certain mineral phases such as tectosilicates (quartz and feldspar), some oxides, phosphates and sulfides (Krupnik and Khan, 2019). Moreover, spectral analyses are commonly based on chemometrics which, to overcome the absence of well-defined peaks, handle the entire range of wavelengths. Here, we use a PLS regression to assess the relationship between the DRIFTS-inferred mineral abundances and core image spectra, because the PLS regression allows us to assess the accuracy of the calibration. The analysis of PLS regression coefficients is commonly used to evaluate the performance of prediction models (Vogel et al., 2008; Hahn et al., 2011). Models relying on direct relationships between the investigated minerals and the

448 spectra (such as the SWIR-HSI models for calcite and clay minerals) are considered reliable and
449 replicable because absorbance is directly influenced by specific functional bands in the crystalline
450 structure of the minerals (Hahn et al., 2011, 2018). In contrast, models based on indirect relationships
451 (such as the SWIR-HSI model for quartz) rely on inter-correlations between different mineralogical or
452 physical properties that occur in specific sedimentological configurations and may, therefore, not be
453 replicable elsewhere. In the present study, the good SWIR-HSI predictions of calcite and clay
454 minerals result from a direct relationship to their respective functional groups. In the case of the clays,
455 the correlation (> 0.60) that exists between clay minerals and clay-silt texture and hydroxyl bonds (see
456 section 4.4.1, Table 3) may not result from intrinsic spectral properties of the clays, but rather from
457 grain-size and moisture effects affecting the SWIR spectra. Nonetheless, dried and ground samples
458 yield DRIFTS-derived abundance trends and values that are similar to that of the SWIR data implying
459 that the SWIR-HSI prediction of clay minerals is mainly based on their spectral functional bonds, not
460 by grain-size or moisture in the core. Similarly calcite predictions show no correlations with the
461 physical properties of the core. By contrast, the acceptable prediction of quartz abundance by SWIR-
462 HSI cannot result from the direct measurement of functional groups, as they do not reflect in that
463 spectral range (see section 4.2.3.). The SWIR-HSI predicted quartz show significant positive
464 correlations (> 0.60) with fine and total sand fractions (Table 3) and negative correlations (< -0.6) with
465 the clay minerals. Moreover, the raw PLSR coefficients of quartz are negatively correlated (-0.82) with
466 the calcite coefficients (Fig. 7). Therefore, quartz prediction by SWIR-HSI is made successful here
467 owing to its close association to a fine and medium sand characterized by a relatively low calcite and
468 clay mineral content, as opposed to silty-clay (rich of clay minerals) or shelly (rich of calcite) sediment
469 with more heterogeneous textures. This association between well sorted, fine-to medium sand, and
470 abundant quartz is a common characteristics of sediments that however is far from systematic.
471 Therefore, the use of the methodology should be conducted with care, with a substantial site-specific
472 foreknowledge of the sediment composition and of its variations. Used inappropriately, the model will
473 generate significant inaccuracies.
474
475 **5.3. Two-sensors infrared approach: complementarity, advantages and limits.**
476 The two-sensor approach relies on the near- and mid-infrared electromagnetic ranges (Fig. 5).
477 DRIFTS provides a precise quantification of quartz, calcite and clay minerals content owing to its high

sensitivity to specific functional bands in the mid-infrared range: O-H, N-H, C-H stretching, H-O-H deformation, CO_3, Si-O stretching, Si-O-Al and Fe-O (Russell & Fraser, 1994; Chukanov & Chervonnyi, 2016). The use of dried, ground samples ensures homogeneity and replicability of measurements. The analysis does not alter the chemistry and mineralogy of the samples, which can therefore be reused in other analyses. Compared to X-Ray Diffraction, DRIFTS is less sensitive to mineral phases present in small amount. However, is not subject to analytical biases introduced by the differential settling or preferred orientations of minerals (Herbert et al., 1992). Besides, owing to its wide range of wavenumbers (from 4.000 to 450 cm^{-1}), DRIFTS provides good qualitative determination of clay minerals directly on bulk sediments and it is sensitive to both amorphous silica (Meyer-Jacob et al., 2014; Frohlich, 1989) and organic compounds (Francos et al., 2021; Chapman et al., 2001). Therefore, it constitutes a relevant alternative to conventional XRD for the calibration of mineral abundance based on hyperspectral images (Greene et al., 2019). To conduct an optimal HSI modelling, calibration samples should cover the entire range of mineral concentrations (Vogel et al., 2008), which is found in the image. To capture the expected range, samples should be collected at regular, and rather short depth-intervals along the core, generating a sizeable number of samples. To process such a large number of samples, DRIFTS is also appropriate because it can be carried out on small (10 mg) samples, because it do not involve hazardous chemical materials nor dangerous radiation emissions. Sample preparation is quick (~1 min/sample) and simple. The establishment of the calibration curves using synthetic mixtures is the most time-consuming step, but future users can simply reuse the linear regression coefficients provided in this study in order to obtain (semi) quantitative mineral abundances from the DRIFT spectra of natural sediments.

Although near-infrared spectra obtained by hyperspectral core-imaging are less sensitive to mineral composition and not sensitive to tectosilicates, they provide unprecedented time-saving (2 min/meter), high-resolution investigations (185 μm^2 pixel) in a completely non-invasive and non-destructive manner. The main challenges arise from the irregular and heterogeneous state of the sediment core surface, which often presents particle size and humidity variations that strongly impact the near infrared spectrum, leading to prediction bias (Verpoorter et al., 2014). For this reason, calibrations with mineral abundance values inferred by the DRIFTS on powdered and dry samples constraint the PLSR algorithm to specific-absorbance of minerals and reduce the effects of moisture and grain-size. The latter can be easily detected using two main absorptions bands by O-H bonds around 1,440 nm

508 and 1,925 nm, but also by the rise of the spectra baseline in the Near- and Mid-Infrared ranges (Fig
509 5). In the present study, low deviations between DRIFTS-inferred and SWIR-HSI predictions of
510 minerals (< 1.5, see section 4.4.2.) suggest that the heterogeneous grain-size state of the sediment
511 core surface is overcome by the PLSR modelling. By contrast, the prediction of quartz remains
512 strongly dependent of site-specific sediment and mineralogical characteristics.
513
514 **5.4. Depositional environments encountered along core ALB-1**
515
516 The palaeovalley of the Albegna River has been incised during the last glacial sea-level low stands; it
517 was subsequently infilled by marine and fluvial sediments during the Late-glacial to Holocene
518 transgression (Mazzini et al., 1999). The delta of the Albegna River has progressively prograded and
519 filled its valley, while a sand-spit was building up farther offshore, progressively isolating a lagoon
520 from the open sea. The delta is therefore expected to have grown first in an open marine
521 environment, and then in a lagoonal environment, before reaching the sand spit and shedding its
522 sediment, along the sand spit foreshore. The core is located within the former lagoon, immediately
523 behind the sand spit, at a location that probably emerged just as the emerged delta floodplain was
524 reaching the sand spit,
525 Non-continuous grain-size analysis, continuous magnetic susceptibility, and mineral core-logging
526 reveal three stratigraphic units, which we subdivided into two-three sub-units (Fig. 3). The lower
527 sequence SU1 contains thin (1 cm-thick) silty-clay layers interbedded with fine- to medium- grained,
528 quartz-rich sand containing occasional shells and well-rounded gravel. Considering its age (> 5,300
529 BCE), unit SU1 can be interpreted as deposited in an open marine environment, during the
530 transgression and maximum flooding of the Albegna palaeo-valley. The slight upward coarsening,
531 from SU1-A to SU1-B, may reflect the progradation of the Albegna River delta (Styllas, 2014) after the
532 maximum flooding. It is associated with a slight but continuous increase in quartz abundance, which
533 may result from the positive correlation between quartz abundance and sand grain size. The
534 continuous record (Fig. 3D) reveals an abrupt superposition of the overlying deposits (SU2-1),
535 composed of organic clays. This facies is reminiscent of the quiet lagoonal environment still found
536 today in the remain parts of the lagoon, and is therefore interpreted as resulting from the rapid
537 development of lagoonal conditions behind the sand spit (5,500 to 5,370 BCE) during the Atlantic.

This unit is overlaid by extremely heterogeneous sediments (SU2-B) consisting of fine- to medium-grained sand deposits interbedded with silty-clayey layers. Calcite content is at its highest and correlates with layers of medium- to coarse-grained sand made of shell fragments. This facies indicates a highly biologically productive in the shallow lagoon occurring between 4,240 and 4,000 BCE) at the end of the Atlantic. The greater abundance of sand, compared to the lagoon of Orbetello farther south, indicates the proximity of either an inlet in the sand spit, or/and, most likely, the increasing proximity of the Albegna River mouth, as the river delta progrades across the lagoon toward the coring site. Local peaks in magnetic susceptibility are produced by gravely beds rich in shell fragments and may represent the reworking of the coarsest river sediments. The SU2-B to SU2-C evolution from a reducing to oxidizing environment (grey to brown-colored sediments) and the increase in grain-size (from fine-medium- to coarse-grained sand) reflects the progressive shoaling of the lagoon, as the Albegna River mouth gets closer to the coring site. The highest unit (SU3) is composed of emerged floodplain sediments, deposited on the banks of the Albegna River, once the coring site had been integrated into its delta plain between 2,880 and 2,630 cal BC, during the Subboreal. The overbank deposits consist of weathered silty-clay, rich in clay minerals, cemented by carbonate concretions deposited near the water table. The top of the core (SU3-B) consists of dark-brown silty-clay and unsorted sands. Its dark brownish color may reflect more advanced pedogenesis, in a floodplain progressively less frequently subjected to flooding. However, interpretation is made difficult by the fact that this sediment has been strongly reworked by anthropogenic activity, which is attested by the high density of Roman sherds in this top unit.

5.5. Wider significance

The widespread use of sediment cores for a variety of environmental research, mining and civil engineering applications provides a favorable context for the development of fast techniques that do not require time-consuming pretreatments with chemical products. The need for fast and easily applied techniques encourages approaches based on continuous core-logging calibrated on punctual analyses (Greene et al., 2019). The two-sensor infrared methodology proposed here, involving DRIFTS and SWIR-HSI for the continuous logging of mineral abundances along sediment cores, provides a simple and time-saving approach. Hyperspectral imaging has already demonstrated its added value in the study of lacustrine environments (Sorrel et al., 2021; Makri et al., 2020; Butz et al.,

2017; Aymerich et al., 2016). Its application to a wider range of sedimentary environments remains to be tested, especially in contexts, such as here, where substantial grain-size variations occur along core. Here our combined two infrared sensor approach shows sharp mineralogical variations between subunits and within subunits. The maps of mineral abundances provide extremely high-resolution horizontal and vertical values of abundances, highlighting laminations and the fine-scale architecture of the sediment layers. Our analysis, albeit restricted to three major mineral species and groups, illustrates variations that can be tied to major changes in the depositional environment (open sea, lagoonal, fluvio-deltaic). We believe that the high resolution prediction of calcite and clay minerals could be easily applied in other sedimentological environments, but for prediction of quartz we rather recommend to use Mid-Wave InfraRed (MWIR: 2,700-5,300 nm) or Long-Wave InfraRed (LWIR: 8,000-12,000 nm) hyperspectral cameras (Contreras Acosta et al., 2020; Lorenz et al., 2019) that are sensible to tectosilicates. To improve processing times, benchtop DRIFTS measurements could be replaced by the emerging hand-operated FTIR, but the use of such non-destructive techniques has to reckon with issues of sample humidity and grainsize variations at the sediment surface. Wider significance of this approach would be found in geoarchaeological stratigraphy (Haburaj et al., 2020; Linderholm et al., 2018) and sequence stratigraphy where hyperspectral imaging could be correlated with Ground Penetrating Radar (GPR) profiles. Moreover, in palaeo-lagoon investigations correlated with seasonal variations of macro- and micro-fauna.

6. Conclusion

This study demonstrates the potential of a two-sensor infrared methodology involving Diffuse Reflectance Infrared Fourier Transform spectroscopy (DRIFTS) and Short-Wave InfraRed (SWIR) hyperspectral imaging (HSI) to provide a simple and time-saving approach for continuous logging of mineral abundances along sediment cores. The DRIFT spectra were used to provide quantitative estimations for quartz, calcite and clay minerals abundances of single and multi-phase synthetic mixtures. Therefore, reliable DRIFTS-inferred estimations of these minerals were obtained for 60 sediment samples from a 14 meters-depth core (ALB-1), drilled in the deltaic deposits of the Albegna River. The mineral abundance values were fused with the SWIR-HSI data in order to establish partial least squares regression (PLSR) model aiming to assign continuous logging of mineral abundances

along the ALB-1 core. The PLSR statistical performance was satisfactory showing high degree of agreement between the DRIFT-induced and SWIR-HSI predicted results. The same predicting model was used to compute maps of mineral abundances evidencing the layered structure of mineral concentrations. The classical sedimentological non-continuous analyses (e.g. grain-size), complemented by combined DRIFTS and SWIR-HSI approach, bring into focus changes of sediment dynamics and depositional patterns recorded into the deltaic facies at high-resolution vertical scale. We contend here that the fused two-sensor infrared approach has a clear potential to help reconstructing fluvial-deltaic sedimentary successions. Calcite and clay minerals could be reliably predicted in other sedimentary environments. However, in terms of quartz prediction, the SWIR-HSI remain limited and it cannot be used for direct spectra modeling of tectosilicates. To overcome this issue, we rather recommend to use Mid-Wave InfraRed (MWIR: 2,700-5,300 nm) or Long-Wave InfraRed (LWIR: 8,000-12,000 nm) hyperspectral cameras. However, these latter significantly costlier. Further analyses are intended in order to provide quantifications of specific phyllosilicates (kaolinite vs. illite vs. smectite) by DRIFTS in order to test whether they could be reliably predicted by SWIR-HSI in complex fluvio-deltaic sediment mixtures. Moreover, research involving DRIFT-induced total organic matter and biogenic silica abundances are currently in progress in order to provide a wider understanding of the total sample composition.

7. Acknowledgement

This research was conducted in the framework of the IDEX-Lyon Scientific Breakthrough Program: "*Thalassocraties sans ports: fait ou fiction?"* directed by Jean-Philippe Goiran and funded by the National Agency for Research. Further financial assistance came from the Mobility program SMI-INSHS-CNRS and LabEx IMU programe: URBO, led by Jean-Philippe Goiran. The Alexander von Humboldt Foundation, Germany, generously accorded additional funding to the project and Andrea U. De Giorgi. The study is conducted in close cooperation with the *Soprintendenza Archeologica Belle Arti e Paesaggio per le Province di Siena, Grosseto e Arezzo,* the World Wide Fund for Nature (WWF Oasi), the Municipality of Orbetello and the French National Centre for Scientific Research CNRS. The equipment and facilities permitting DRIFTS measurements were co-founded by the LabCom Geo-Heritage (ANR-15-LCV4-0002), University of Lyon 2, IDEX-Lyon Scientific Breakthrough Program, European Research Council (Grant Agreement 339123) and the University of Paris 1

628 Pantheon-Sorbonne. The hyperspectral imaging acquisition was made at the University of
629 Normandie-Rouen and was funded by the Region Normandie, which supports the scientific
630 consortium SCALE UMR CNRS 3730. The authors are grateful to Dr. Matteo Milletti and Salvatore
631 Russo for their help at the field in the *Torre Saline* Area as well, Mauro and Barbara for their help with
632 the accommodation, Maureen le Doaré for the stratigraphic computer assistant drawing and Maël
633 Ogier for the help with the wet sieving and magnetic susceptibility measurements. The authors thank
634 gratefully the two anonymous reviewers for their constructive and detailed feedbacks permitting to
635 improve earlier versions of this manuscript.
636
637 8. Data Availability
638 All the data that support the findings of this study are available from the corresponding author upon
639 reasonable request.
640
641 References
642 Andrews, J. T., & Eberl, D. D. 2012. Determination of sediment provenance by unmixing the mineralogy
643 of source-area sediments: the “SedUnMix” program. Marine Geology, 291, 24-33.
644 Aymerich, I. F., Oliva, M., Giralt, S., & Martín-Herrero, J. 2016. Detection of tephra layers in Antarctic
645 sediment cores with hyperspectral imaging. PLoS One, 11(1), e0146578.
646 Bandopadhyay, A. K. 2010. Determination of quartz content for Indian coals using an FTIR technique.
647 International Journal of Coal Geology, 81(1), 73-78.
648 Bertaux, J., Froehlich, F., & Ildefonse, P. 1998. Multicomponent analysis of FTIR spectra; quantification
649 of amorphous and crystallized mineral phases in synthetic and natural sediments. Journal of
650 Sedimentary Research, 68(3), 440-447.
651 Bertoni, D., Giacomelli, S., Ciulli, L., & Sarti, G. 2020. Litho-sedimentological and morphodynamic
652 characterization of the Pisa Province coastal area (northern Tuscany, Italy). *Journal of*
653 *Maps*, *16*(2), 108-116.
654 Bertini, M., Cocozza, T., Signorini, R. 1967. Carta geologica d’Italia, Orbetello, Foglio 135, Ser. Geol.
655 Italia.
656 Bigus, P., Tobiszewski, M., & Namieśnik, J. 2014. Historical records of organic pollutants in sediment
657 cores. Marine pollution bulletin, 78(1-2), 26-42.

658 Bosch-Reig, F., Gimeno-Adelantado, J. V., Bosch-Mossi, F., & Doménech-Carbó, A. 2017. Quantification
659 of minerals from ATR-FTIR spectra with spectral interferences using the MRC method.
660 Spectrochimica Acta Part A: Molecular and Biomolecular Spectroscopy, 181, 7-12.
661 Bossio, A., Foresi, L. M., Mazzei, R., Salvatorini, G., Sandrelli, F., Bilotti, M., ... & Rossetto, R. 2003.
662 Geology and stratigraphy of the southern sector of the Neogene Albegna River Basin (Grosseto,
663 Tuscany, Italy). Geologica Romana, 37(2003-2004), 165-173.
664 Butz, C., Grosjean, M., Goslar, T., & Tylmann, W. 2017. Hyperspectral imaging of sedimentary bacterial
665 pigments: a 1700-year history of meromixis from varved Lake Jaczno, northeast Poland. Journal of
666 Paleolimnology, 58(1).
667 Chapkanski, S., Ertlen, D., Rambeau, C., & Schmitt, L. 2020. Provenance discrimination of fine
668 sediments by mid-infrared spectroscopy: Calibration and application to fluvial palaeo-
669 environmental reconstruction. Sedimentology, 67(2), 1114-1134.
670 Chapman, S. J., Campbell, C. D., Fraser, A. R., & Puri, G. 2001. FTIR spectroscopy of peat in and
671 bordering Scots pine woodland: relationship with chemical and biological properties. Soil Biology
672 and Biochemistry, 33(9), 1193-1200.
673 Chukanov, N. V., & Chervonnyi, A. D. 2016. Infrared spectroscopy of minerals and related compounds.
674 Springer.
675 Cloutis, E. A. 1989. Spectral reflectance properties of hydrocarbons: Remote-sensing implications.
676 Science, 245(4914), 165–168.
677 Contreras Acosta, I. C., Khodadadzadeh, M., Tolosana Delgado, R., & Gloaguen, R. 2020. Drill-core
678 hyperspectral and geochemical data integration in a superpixel-based machine learning
679 framework. IEEE Journal of Selected Topics in Applied Earth Observations and Remote Sensing,
680 1–16. https://doi.org/10.1109/JSTARS.2020.3011221
681 Cornamusini, G., Foresi, L. M., Massa, G., Bonciani, F., Callegari, I., Da Prato, S., & Ielpi, A. 2011. The
682 Miocene successions of the Fiora Hills: considerations about the development of the minor basins
683 of Southern Tuscany. Italian Journal of Geosciences, 130(3), 404-424.
684 Davies, S. J., Lamb, H. F., & Roberts, S. J. 2015. Micro-XRF core scanning in palaeolimnology: recent
685 developments. Micro-XRF studies of sediment cores, 189-226.
686 Dearing, J. 1999. Environmental magnetic susceptibility using the Bartington MS2 system. Bartington
687 Instruments Ltd. British Library London.

688 Delile, H., Goiran, J. P., & Blichert-Toft, J. 2018. The contribution of geochemistry to ancient harbor
689 geoarcheology: The example of Ostia Antica. Quaternary Science Reviews, 193, 170-187.
690 Duée, C., Orberger, B., Maubec, N., Laperche, V., Capar, L., Bourguignon, A., ... & Koert, P. 2019.
691 Impact of heterogeneities and surface roughness on pXRF, pIR, XRD and Raman analyses:
692 challenges for on-line, real-time combined mineralogical and chemical analyses on drill cores and
693 implication for “high speed” Ni-laterite exploration. Journal of Geochemical Exploration, 198, 1-17.
694 Fernandes, K., Júnior, J. M., de Souza Bahia, A. S. R., Demattê, J. A., & Ribon, A. A. 2020. Landscape-
695 scale spatial variability of kaolinite-gibbsite ratio in tropical soils detected by diffuse reflectance
696 spectroscopy. Catena, 195, 104795.
697 Francos, N., Ogen, Y., & Ben-Dor, E. 2021. Spectral assessment of organic matter with different
698 composition using reflectance spectroscopy. Remote Sensing, 13(8), 1549.
699 Frei, R. W., & MacNeil, J. D. 2019. Diffuse reflectance spectroscopy in environmental problem-solving.
700 CRC press.
701 Fröhlich, F. (1989). Deep-sea biogenic silica: new structural and analytical data from infrared analysis-
702 geological implications. Terra nova, 1(3), 267-273.
703 Garzanti, E., Andó, S., France-Lanord, C., Censi, P., Vignola, P., Galy, V., & Lupker, M. 2011.
704 Mineralogical and chemical variability of fluvial sediments 2. Suspended-load silt (Ganga–
705 Brahmaputra, Bangladesh). Earth and Planetary Science Letters, 302(1-2), 107-120.
706 Garzanti, E., Andò, S., France-Lanord, C., Vezzoli, G., Censi, P., Galy, V., & Najman, Y. 2010.
707 Mineralogical and chemical variability of fluvial sediments: 1. Bedload sand (Ganga–Brahmaputra,
708 Bangladesh). Earth and Planetary Science Letters, 299(3-4), 368-381.
709 Ghanbari, H., Jacques, O., Adaïmé, M. É., Gregory-Eaves, I., & Antoniades, D. 2020. Remote Sensing of
710 Lake Sediment Core Particle Size Using Hyperspectral Image Analysis. Remote Sensing, 12(23),
711 3850.
712 Gliozzo, E., Iacoviello, F., & Foresi, L. M. 2014. Geosources for ceramic production: The clays from the
713 Neogene–Quaternary Albegna Basin (southern Tuscany). Applied clay science, 91, 105-116.
714 Greene, J., Kosanke, T. H., & Linton, P. EA. 2019. Quantitative Calibration of Hyperspectral Core
715 Imaging Data: A New Method for Producing Continuous, High-Resolution Mineralogical
716 Characterization of Cores from Both Conventional and Unconventional Reservoirs. Annual
717 Convention and Exhibition (AAPG). 0-20.

718 Haburaj, V., Japp, S., Gerlach, I., Hoelzmann, P., & Schütt, B. 2020. Coupling spectral imaging and
719 laboratory analyses to digitally map sediment parameters and stratigraphic layers in Yeha,
720 Ethiopia. Plos one, 15(9), e0238894.
721 Hahn, A., Gerdts, G., Völker, C., & Niebühr, V. 2019. Using FTIRS as pre-screening method for detection
722 of microplastic in bulk sediment samples. Science of the total environment, 689, 341-346.
723 Hahn, A., Rosen, P., Kliem, P., Ohlendorf, C., & Zolitschka, B. 2011. Comparative study of infrared
724 techniques for fast biogeochemical sediment analyses. Geochemistry, Geophysics, Geosystems,
725 12(10).
726 Hahn, A., Vogel, H., Andó, S., Garzanti, E., Kuhn, G., Lantzsch, H., Schuurman J., Vogt C., & Zabel, M.
727 2018. Using Fourier transform infrared spectroscopy to determine mineral phases in
728 sediments. Sedimentary geology, 375, 27-35.
729 Hamdan, M. A., Hassan, F. A., Flower, R. J., Leroy, S. A. G., Shallaly, N. A., & Flynn, A. 2019. Source of
730 Nile sediments in the floodplain at Saqqara inferred from mineralogical, geochemical, and pollen
731 data, and their palaeoclimatic and geoarchaeological significance. Quaternary international, 501,
732 272-288.
733 He, J., Garzanti, E., Dinis, P., Yang, S., & Wang, H. 2020. Provenance versus weathering control on
734 sediment composition in tropical monsoonal climate (South China)-1. Geochemistry and clay
735 mineralogy. Chemical Geology, 558, 119860.
736 Henry, D. G., Watson, J. S., & John, C. M. 2017. Assessing and calibrating the ATR-FTIR approach as a
737 carbonate rock characterization tool. Sedimentary geology, 347, 36-52.
738 Herbert, T. D., Tom, B. A., & Burnett, C. 1992. Precise major component determinations in deep-sea
739 sediments using Fourier Transform Infrared Spectroscopy. Geochimica et Cosmochimica Acta,
740 56(4), 1759-1763.
741 Heroy, D. C., Kuehl, S. A., & Goodbred Jr, S. L. 2003. Mineralogy of the Ganges and Brahmaputra
742 Rivers: implications for river switching and Late Quaternary climate change. Sedimentary Geology,
743 155(3-4), 343-359.
744 Jacq, K., Giguet-Covex, C., Sabatier, P., Perrette, Y., Fanget, B., Coquin, D., Debret, M., & Arnaud, F.
745 (2019). High-resolution grain size distribution of sediment core with hyperspectral imaging.
746 Sedimentary Geology, 393, 105536.

747 Jacq, K., Martinez-Lamas, R., Van Exem, A., & Debret, M. 2020. Hyperspectral core-logger image
748 acquisition. In Protocols.io. https://protocols.i/view/hyperspectral-core-logger-image-acquisition-
749 bikckcsw
750 Jacq, K., Perrette, Y., Fanget, B., Sabatier, P., Coquin, D., Martinez-Lamas, R., Debret, M., & Arnaud, F.
751 2019. High-resolution prediction of organic matter concentration with hyperspectral imaging on a
752 sediment core. Science of the Total Environment, 663, 236-244.
753 Joussein, E., Petit, S., & Decarreau, A. 2001. Une nouvelle méthode de dosage des minéraux argileux
754 en mélange par spectroscopie IR. Comptes Rendus de l'Académie des Sciences-Series IIA-Earth
755 and Planetary Science, 332(2), 83-89.
756 Kahraman, S., Rostami, J., & Naeimipour, A. 2016. Review of ground characterization by using
757 instrumented drills for underground mining and construction. Rock Mechanics and Rock
758 Engineering, 49(2), 585-602.
759 Kelsey, H. M., Engelhart, S. E., Pilarczyk, J. E., Horton, B. P., Rubin, C. M., Daryono, M. R., Ismail, N.,
760 Hawkes, A. D., Bernhardt, C. E., & Cahill, N. 2015. Accommodation space, relative sea level, and
761 the archiving of paleo-earthquakes along subduction zones. Geology, 43(8), 675-678.
762 Krupnik, D., & Khan, S. (2019). Close-range, ground-based hyperspectral imaging for mining applications
763 at various scales: Review and case studies. Earth-Science Reviews, 198, 34.
764 https://doi.org/10.1016/j.earscirev.2019.102952
765 Larkin, P. 2017. Infrared and Raman spectroscopy: principles and spectral interpretation. Elsevier.
766 Li, J., Hu, B., Wei, H., Zhao, J., Zou, L., Bai, F., Dou, Y., Wang, L., & Fang, X. 2014. Provenance
767 variations in the Holocene deposits from the southern Yellow Sea: clay mineralogy evidence.
768 Continental Shelf Research, 90, 41-51.
769 Linderholm, J., Geladi, P., Gorretta, N., Bendoula, R., & Gobrecht, A. 2019. Near infrared and
770 hyperspectral studies of archaeological stratigraphy and statistical
771 considerations. Geoarchaeology, 34(3), 311-321.
772 Liu, J., Zhang, J., Miao, X., Xu, S., & Wang, H. 2020. Mineralogy of the core YRD-1101 of the Yellow
773 River Delta: Implications for sediment origin and environmental evolution during the last~ 1.9 Myr.
774 Quaternary International, 537, 79-87.
775 Lorenz, S., Seidel, P., Ghamisi, P., Zimmermann, R., Tusa, L., Khodadadzadeh, M., Contreras, I. C., &
776 Gloaguen, R. 2019. Multi-Sensor Spectral Imaging of Geological Samples: A Data Fusion

777 Approach Using Spatio-Spectral Feature Extraction. Sensors, 19(12), 2787.
778 https://doi.org/10.3390/s19122787
779 Lupker, M., France-Lanord, C., Galy, V., Lavé, J., Gaillardet, J., Gajurel, A. P., Guilmette, C., Rahman,
780 M., Singh, S. K., & Sinha, R. 2012. Predominant floodplain over mountain weathering of
781 Himalayan sediments (Ganga basin). Geochimica et Cosmochimica Acta, 84, 410-432.
782 Madejova, J., & Komadel, P. 2001. Baseline studies of the clay minerals society source clays: infrared
783 methods. Clays and clay minerals, 49(5), 410-432.
784 Madejová, J., Gates, W.P., Petit, S. 2017. IR Spectra of Clay Minerals. In: Developments in Clay Science
785 107–149.
786 Makri, S., Rey, F., Gobet, E., Gilli, A., Tinner, W., & Grosjean, M. 2020. Early human impact in a 15,000-
787 year high-resolution hyperspectral imaging record of paleoproduction and anoxia from a varved
788 lake in Switzerland. Quaternary science reviews, 239, 106335.
789 Makri, S., Rey, F., Gobet, E., Gilli, A., Tinner, W., & Grosjean, M. 2020. Early human impact in a 15,000-
790 year high-resolution hyperspectral imaging record of paleoproduction and anoxia from a varved
791 lake in Switzerland. Quaternary science reviews, 239, 106335.
792 Märker, M., Angeli, L., Bottai, L., Costantini, R., Ferrari, R., Innocenti, L., & Siciliano, G. 2008.
793 Assessment of land degradation susceptibility by scenario analysis: A case study in Southern
794 Tuscany, Italy. Geomorphology, 93(1-2), 120-129.
795 Martinelli, L. A., Victoria, R. L., Dematte, J. L. I., Richey, J. E., & Devol, A. H. 1993. Chemical and
796 mineralogical composition of Amazon River floodplain sediments, Brazil. Applied Geochemistry,
797 8(4), 391-402.
798 Mazzini, I., Anadon, P., Barbieri, M., Castorina, F., Ferreli, L., Gliozzi, E., Mola, M., & Vittori, E. (1999).
799 Late Quaternary sea-level changes along the Tyrrhenian coast near Orbetello (Tuscany, central
800 Italy): palaeoenvironmental reconstruction using ostracods. Marine Micropaleontology, 37(3-4),
801 289-311.
802 Melucci, D., Zappi, A., Poggioli, F., Morozzi, P., Giglio, F., & Tositti, L. 2019. ATR-FTIR spectroscopy, a
803 new non-destructive approach for the quantitative determination of biogenic silica in marine
804 sediments. Molecules, 24(21), 3927.

805 Meyer-Jacob, C., Vogel, H., Boxberg, F., Rosén, P., Weber, M. E., & Bindler, R. 2014. Independent
806 measurement of biogenic silica in sediments by FTIR spectroscopy and PLS regression. Journal of
807 paleolimnology, 52(3), 245-255.
808 Miller, C., Hahn, A., Liebrand, D., Zabel, M., & Schefuß, E. 2020. Mid-and low latitude effects on eastern
809 South African rainfall over the Holocene. Quaternary Science Reviews, 229, 106088.
810 Milosevic, M. (2012). Internal reflection and ATR spectroscopy (Vol. 176). John Wiley & Sons.
811 Moore, D. M., & Reynolds Jr, R. C. 1989. X-ray Diffraction and the Identification and Analysis of Clay
812 Minerals. Oxford University Press (OUP).
813 Moosavi, S. M., & Ghassabian, S. 2018. Linearity of calibration curves for analytical methods: A review of
814 criteria for assessment of method reliability. Calibration and Validation of Analytical Methods: A
815 Sampling of Current Approaches; IntechOpen Limited: London, UK, 109-127.
816 Moros, J., Vallejuelo, S. F. O. D., Gredilla, A., Diego, A. D., Madariaga, J. M., Garrigues, S., & Guardia,
817 M. D. L. 2009. Use of reflectance infrared spectroscopy for monitoring the metal content of the
818 estuarine sediments of the Nerbioi-Ibaizabal River (Metropolitan Bilbao, Bay of Biscay, Basque
819 Country). Environmental science & technology, 43(24), 9314-9320.
820 Müller, C. M., Pejcic, B., Esteban, L., Delle Piane, C., Raven, M., & Mizaikoff, B. 2014. Infrared
821 attenuated total reflectance spectroscopy: an innovative strategy for analyzing mineral
822 components in energy relevant systems. Scientific reports, 4(1), 1-11.
823 Painter, P. C., Coleman, M. M., Jenkins, R. G., Whang, P. W., & Walker Jr, P. L. 1978. Fourier Transform
824 Infrared study of mineral matter in coal. A novel method for quantitative mineralogical analysis.
825 Fuel, 57(6), 337-344.
826 Palmer, K. F., & Williams, D. 1974. Optical Properties of Water in the Near Infrared. Journal of Optical
827 Society of America, 64(8), 1107–1110. https://doi.org/10.1364/JOSA.64.001107
828 Paris, R., Falvard, S., Chagué, C., Goff, J., Etienne, S., & Doumalin, P. 2020. Sedimentary fabric
829 characterized by X-ray tomography: a case-study from tsunami deposits on the Marquesas
830 Islands, French Polynesia. Sedimentology, 67(3), 1207-1229.
831 Pennington, B. T., Sturt, F., Wilson, P., Rowland, J., & Brown, A. G. 2017. The fluvial evolution of the
832 Holocene Nile Delta. Quaternary Science Reviews, 170, 212-231.

833 Pe-Piper, G., Piper, D. J., Wang, Y., Zhang, Y., Trottier, C., Ge, C., & Yin, Y. 2016. Quaternary evolution
834 of the rivers of northeast Hainan Island, China: tracking the history of avulsion from mineralogy
835 and geochemistry of river and delta sands. Sedimentary Geology, 333, 84-99.
836 Pichard, C., & Frohlich, F. 1986. Analyses IR quantitatives des sédiments. Exemple du dosage du quartz
837 et de la calcite. Revue de l'Institut français du pétrole, 41(6), 809-819.
838 Pre, C. A. G., Horton, B. P., Kelsey, H. M., Rubin, C. M., Hawkes, A. D., Daryono, M. R., Rosenberg, G.,
839 & Culver, S. J. 2012. Stratigraphic evidence for an early Holocene earthquake in Aceh, Indonesia.
840 Quaternary Science Reviews, 54, 142-151.
841 Rapuc, W., Jacq, K., Develle, A. L., Sabatier, P., Fanget, B., Perrette, Y., Coquin, D., Debret, M.,
842 Wilhelm, B., & Arnaud, F. 2020. XRF and hyperspectral analyses as an automatic way to detect
843 flood events in sediment cores. Sedimentary Geology, 409, 105776.
844 Reimer, P., Austin, W., Bard, E., Bayliss, A., Blackwell, P., Bronk Ramsey, C., Butzin, M., Cheng, H.,
845 Edwards, R., Friedrich, M., Grootes, P., Guilderson, T., Hajdas, I., Heaton, T., Hogg, A., Hughen,
846 K., Kromer, B., Manning, S., Muscheler, R., Palmer, J., Pearson, C., van der Plicht, J., Reimer, R.,
847 Richards, D., Scott, E., Southon, J., Turney, C., Wacker, L., Adolphi, F., Büntgen, U., Capano, M.,
848 Fahrni, S., Fogtmann-Schulz, A., Friedrich, R., Köhler, P., Kudsk, S., Miyake, F., Olsen, J., Reinig,
849 F., Sakamoto, M., Sookdeo, A., & Talamo, S. (2020). The IntCal20 Northern Hemisphere
850 radiocarbon age calibration curve (0–55 cal kBP). Radiocarbon, 62.
851 Rivard, B., Harris, N. B., Feng, J., & Dong, T. 2018. Inferring total organic carbon and major element
852 geochemical and mineralogical characteristics of shale core from hyperspectral imaging. AAPG
853 Bulletin, 102(10), 2101-2121.
854 Robertson, A. J., Shand, C., & Perez-Fernandez, E. 2016. The application of Fourier transform infrared,
855 near infrared and X-ray fluorescence spectroscopy to soil analysis. Spectroscopy Europe, 28(4), 9-
856 13.
857 Rosén, P., Vogel, H., Cunningham, L., Hahn, A., Hausmann, S., Pienitz, R., Zolitschka, B., Wagner, B., &
858 Persson, P. 2011. Universally applicable model for the quantitative determination of lake sediment
859 composition using Fourier transform infrared spectroscopy. Environmental science & technology,
860 45(20), 8858-8865.

Rosén, P., Vogel, H., Cunningham, L., Reuss, N., Conley, D. J., & Persson, P. 2010. Fourier transform infrared spectroscopy, a new method for rapid determination of total organic and inorganic carbon and biogenic silica concentration in lake sediments. Journal of Paleolimnology, 43(2), 247-259.

Rothwell, R. G., & Rack, F. R. 2006. New techniques in sediment core analysis: an introduction. Geological Society, London, Special Publications, 267(1), 1-29.

Russell, J. D., & Fraser, A. R. 1994. Infrared methods. In Clay Mineralogy: Spectroscopic and chemical determinative methods. Springer, Dordrecht. 11-67.

Salomon, F., Goiran, J. P., Noirot, B., Pleuger, E., Bukowiecki, E., Mazzini, I., ... & Germoni, P. (2018). Geoarchaeology of the Roman port-city of Ostia: Fluvio-coastal mobility, urban development and resilience. Earth-Science Reviews, 177, 265-283.

Schulz, B., Sandmann, D., & Gilbricht, S. 2020. SEM-based automated mineralogy and its application in geo-and material sciences. Minerals, 10(11), 1004.

Siebielec, G., McCarty, G. W., Stuczynski, T. I., & Reeves III, J. B. 2004. Near-and mid-infrared diffuse reflectance spectroscopy for measuring soil metal content. Journal of environmental quality, 33(6), 2056-2069.

Solotchina, E. P., Prokopenko, A. A., Kuzmin, M. I., Solotchin, P. A., & Zhdanova, A. N. 2009. Climate signals in sediment mineralogy of Lake Baikal and Lake Hovsgol during the LGM-Holocene transition and the 1-Ma carbonate record from the HDP-04 drill core. Quaternary International, 205(1-2), 38-52.

Sorrel, P., Jacq, K., Van Exem, A., Escarguel, G., Dietre, B., Debret, M., McGowan, S., Ducept, J., Gauthier, E., & Oberhänsli, H. 2021. Evidence for centennial-scale Mid-Holocene episodes of hypolimnetic anoxia in a high-altitude lake system from central Tian Shan (Kyrgyzstan). Quaternary Science Reviews, 252, 106748.

Środoń, J. 2002. Quantitative mineralogy of sedimentary rocks with emphasis on clays and with applications to K-Ar dating. Mineralogical Magazine, 66(5), 677-687.

Styllas, M. 2014. A simple approach to define Holocene sequence stratigraphy using borehole and cone penetration test data. Sedimentology, 61(2), 444-460.

Tamburini, F., Adatte, T., Föllmi, K., Bernasconi, S. M., & Steinmann, P. 2003. Investigating the history of East Asian monsoon and climate during the last glacial–interglacial period (0–140 000 years):

890 mineralogy and geochemistry of ODP Sites 1143 and 1144, South China Sea. Marine Geology,
891 201(1-3), 147-168.
892 Van Exem, A., Debret, M., Copard, Y., Verpoorter, C., De Wet, G., Lecoq, N., Sorrel, P., Werner, A.,
893 Roof, S., Laignel, B., & Retelle, M. 2019. New source-to-sink approach in an arctic catchment
894 based on hyperspectral core-logging (Lake Linné, Svalbard). Quaternary Science Reviews, 203,
895 128-140.
896 Verpoorter, C., Carrère, V., & Combe, J.-P. 2014. Visible, near-infrared spectrometry for simultaneous
897 assessment of geophysical sediment properties (water and grain size) using the Spectral
898 Derivative-Modified Gaussian Model. Journal of Geophysical Research: Earth Surface, 119(10),
899 2098–2122. https://doi.org/10.1002/2013JF002969
900 Viscarra Rossel, R. A., & Behrens, T. 2010. Using data mining to model and interpret soil diffuse
901 reflectance spectra. Geoderma, 158(1–2), 46–54. https://doi.org/10.1016/j.geoderma.2009.12.025
902 Vogel, H., Meyer-Jacob, C., Thöle, L., Lippold, J. A., & Jaccard, S. L. 2016. Quantification of biogenic
903 silica by means of Fourier transform infrared spectroscopy (FTIRS) in marine sediments.
904 Limnology and oceanography: methods, 14(12), 828-838.
905 Vogel, H., Rosén, P., Wagner, B., Melles, M., & Persson, P. 2008. Fourier transform infrared
906 spectroscopy, a new cost-effective tool for quantitative analysis of biogeochemical properties in
907 long sediment records. Journal of Paleolimnology, 40(2), 689-702.
908 Wahab, H. S. A., & Stanley, D. J. 1991. Clay mineralogy and the recent evolution of the north-central Nile
909 delta, Egypt. Journal of Coastal Research, 317-329.
910 Wan, S., Li, A., Clift, P. D., & Stuut, J. B. W. 2007. Development of the East Asian monsoon:
911 mineralogical and sedimentologic records in the northern South China Sea since 20 Ma.
912 Palaeogeography, Palaeoclimatology, Palaeoecology, 254(3-4), 561-582.
913 Wang, Y., Fan, D., Liu, J. T., & Chang, Y. 2016. Clay-mineral compositions of sediments in the Gaoping
914 River-Sea system: Implications for weathering, sedimentary routing and carbon cycling. Chemical
915 Geology, 447, 11-26.
916 Willis, J. P. 1986. Instrumental analytical techniques in geochemistry: Requirements and applications.
917 Fresenius' Zeitschrift für analytische Chemie, 324(8), 855-864.

Wold, S., Ruhe, A., Wold, H., & Dunn, III, W. J. 1984. The Collinearity Problem in Linear Regression. The Partial Least Squares (PLS) Approach to Generalized Inverses. SIAM Journal on Scientific and Statistical Computing, 5(3), 735–743.

Zaeem, M., Nadeem, M., Pham, T. H., Ashiq, W., Ali, W., Gillani, S. S. M., Moise, E. R. D., Leier, H., Kavanagh, V., Galagedara, L., Cheema, M., & Thomas, R. 2021. Development of a hyperspectral imaging technique using LA-ICP-MS to show the spatial distribution of elements in soil cores. Geoderma, 385, 114831.

Zonta, R., Fontolan, G., Cassin, D., & Dominik, J. 2021. X-ray Computed Tomography as a Tool for Screening Sediment Cores: An Application to the Lagoons of the Po River Delta (Italy). Journal of Marine Science and Engineering, 9(3), 323.

Tables

Table 1: Summary of synthetic mixture showing the mineral %wt by sample.

Table 2:Radiocarbon age determination of the ALB-1 core sediments.

Table 3: Correlation matrix of different mineralogical and physical properties of ALB-1 core sediment samples.

Figures captions

Figure 1: Location map of the Albegna fluvial-deltaic environment at different spatial scales. (A) the Albegna watershed limits and relief, (B) the simplified lithological map of the Albegna watershed and its surroundings and (C) the Albegna low-lying area and the current extensions of the Orbetello lagoon.

Figure 2: Schematic demonstration of the research methodology. Step 1: Scanning of the core by SWIR-HSI; Step 2: Measurement of core samples by DRIFTS; Step 3: Conversion of core sample spectra into mineral abundances; Step 4: Combination of SWIR-HSI and DRIFTS spectra over the area sampled for DRIFTS; Step 5: Calibration of SWIR-HSI data to continuous record of mineral abundances along the core.

Figure 3: Chronostratigraphy of the drill core ALB-1. The figure displays: (A) the texture of sediments, (B) the magnetic susceptibility and grain-size analyses, (C) the mineral abundances %wt by sample,

947 inferred by DRIFT spectroscopy and (D) the high resolution prediction of mineral abundances
948 obtained by the calibrated SWIR-HSI.

949 Figure 4: Overview spectra obtained from the synthetic mixture samples composed of pure minerals
950 and potassium bromide (KBr). The red line highlights the peaks, selected for the establishment of the
951 calibration curves.

952 Figure 5: Descriptive statistics of the short-wave spectra (nm units) obtained by the Hyperspectral
953 Imaging and the mid-infrared spectra (cm-1 units) obtained by the Diffuse Reflectance Infrared Fourier
954 Transform Spectroscopy. Grey lines highlight specific absorbance peaks discussed in this study.
955 Statistics were performed on 60 SWIR-HSI and 60 DRIFTS corresponding spectra of sediment
956 samples along the entire ALB-1 core.

957 Figure 6: Two-dimensional scatter plot of the DRIFT-inferred mineral %wt and the known mineral
958 %wt. The regression line has drowned in black and the confident levels (0.95) in grey. Linear
959 regression equations employed for the mineral %wt estimations are reported.

960 Figure 7: Two-dimensional scatter plot of PLSR-SWIR predicted mineral %wt and the DRIFT-inferred
961 mineral %wt. The PLSR line is drown in black and the confident levels (0.95) in grey. Raw PLSR
962 coefficients for each modeled mineral are reported. Most discriminant coefficients (peaks) are
963 identified and highlighted.

964
965

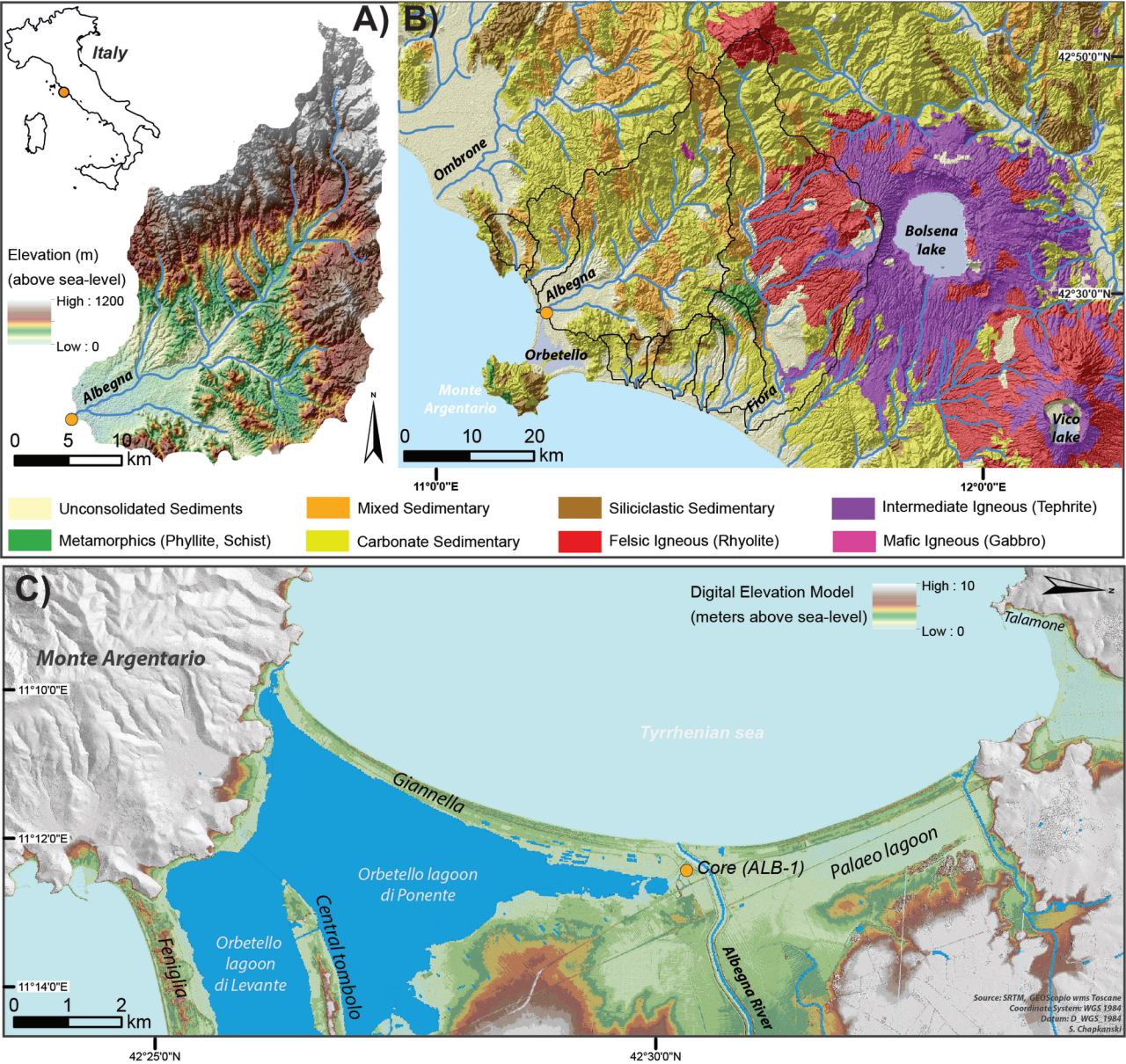
A)
Italy
Elevation (m)
(above sea-level)
High : 1200
Low : 0
Albegna
0 5 10 km
N
B)
Ombrone
Albegna
Orbetello
Monte Argentario
Fiora
Bolsena lake
Vico lake
0 10 20 km
42°50'0"N
42°30'0"N
11°0'0"E
12°0'0"E
Unconsolidated Sediments
Mixed Sedimentary
Siliciclastic Sedimentary
Intermediate Igneous (Tephrite)
Metamorphics (Phyllite, Schist)
Carbonate Sedimentary
Felsic Igneous (Rhyolite)
Mafic Igneous (Gabbro)
C)
Digital Elevation Model
(meters above sea-level)
High : 10
Low : 0
Monte Argentario
Talamone
Tyrrhenian sea
Giannella
Orbetello lagoon di Ponente
Orbetello lagoon di Levante
Central tombolo
Feniglia
Core (ALB-1)
Palaeo lagoon
Albegna River
11°10'0"E
11°12'0"E
11°14'0"E
0 1 2 km
42°25'0"N
42°30'0"N
Source: SRTM, GEOscopio wms Toscane
Coordinate System: WGS 1984
Datum: D_WGS_1984
S. Chapkanski

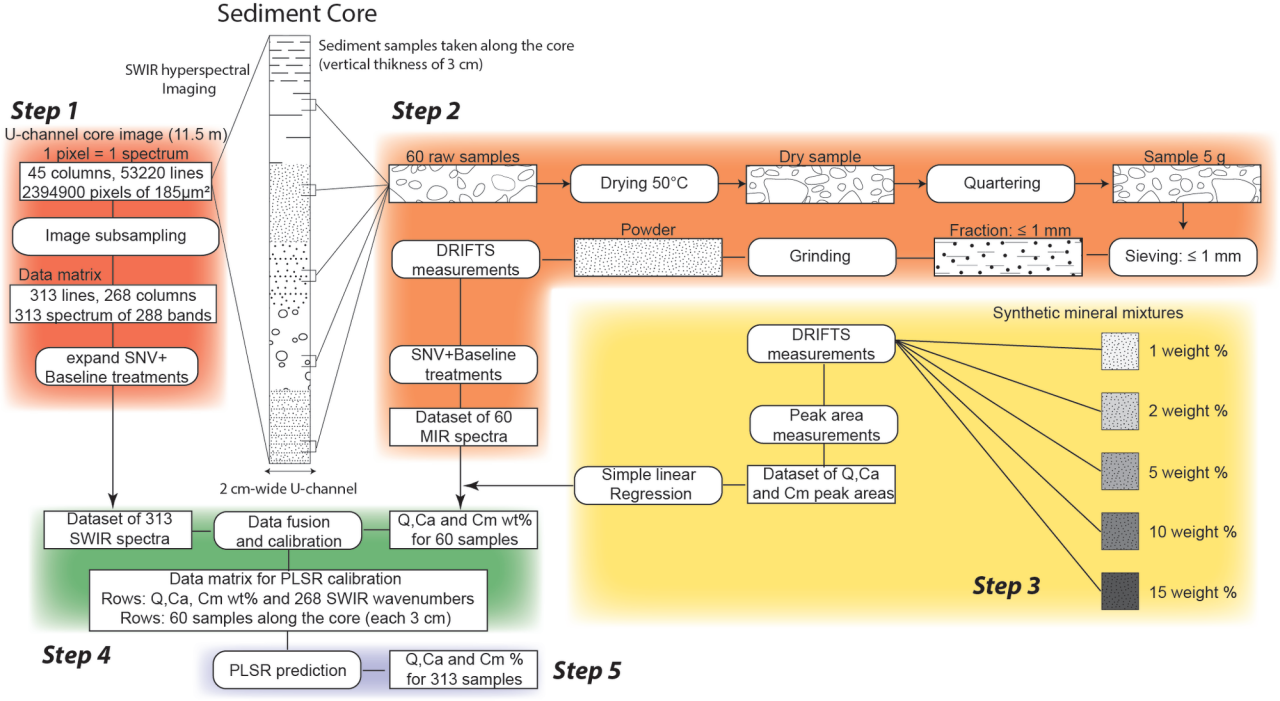
Sediment Core
SWIR hyperspectral Imaging
Sediment samples taken along the core (vertical thikness of 3 cm)
Step 1
U-channel core image (11.5 m)
1 pixel = 1 spectrum
45 columns, 53220 lines
2394900 pixels of 185µm²
Image subsampling
Data matrix
313 lines, 268 columns
313 spectrum of 288 bands
expand SNV+ Baseline treatments
2 cm-wide U-channel
Step 2
60 raw samples
Drying 50°C
Dry sample
Quartering
Sample 5 g
Powder
Grinding
Fraction: ≤ 1 mm
Sieving: ≤ 1 mm
DRIFTS measurements
SNV+Baseline treatments
Dataset of 60 MIR spectra
Synthetic mineral mixtures
DRIFTS measurements
1 weight %
2 weight %
5 weight %
10 weight %
15 weight %
Peak area measurements
Dataset of Q,Ca and Cm peak areas
Simple linear Regression
Step 3
Dataset of 313 SWIR spectra
Data fusion and calibration
Q,Ca and Cm wt% for 60 samples
Data matrix for PLSR calibration
Rows: Q,Ca, Cm wt% and 268 SWIR wavenumbers
Rows: 60 samples along the core (each 3 cm)
Step 4
PLSR prediction
Q,Ca and Cm % for 313 samples
Step 5

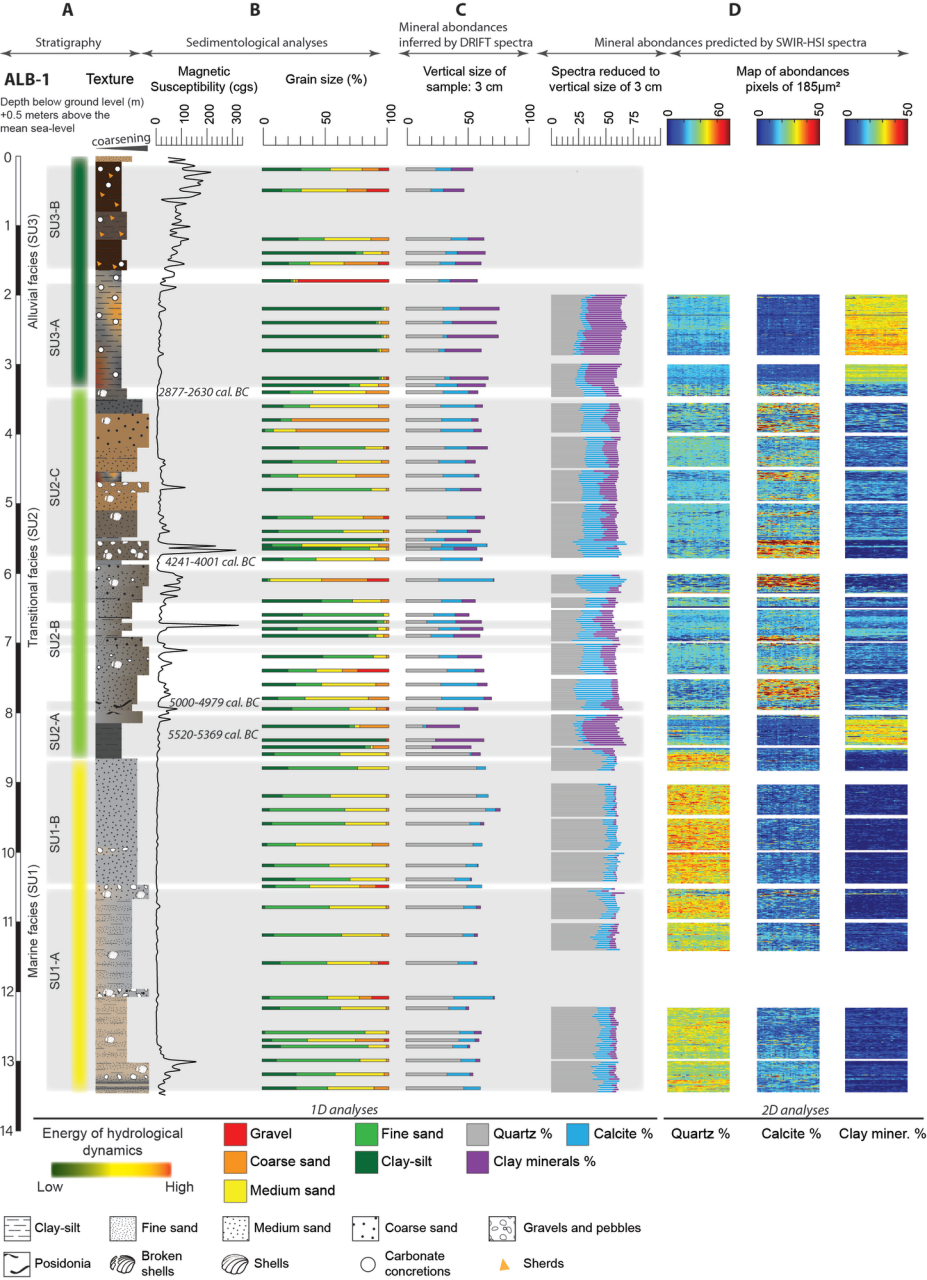
A
Stratigraphy
B
Sedimentological analyses
C
Mineral abondances inferred by DRIFT spectra
D
Mineral abondances predicted by SWIR-HSI spectra
ALB-1
Texture
Depth below ground level (m)
+0.5 meters above the mean sea-level
coarsening
Magnetic Susceptibility (cgs)
Grain size (%)
Vertical size of sample: 3 cm
Spectra reduced to vertical size of 3 cm
Map of abondances pixels of 185µm²
Alluvial facies (SU3)
Transitional facies (SU2)
Marine facies (SU1)
SU3-B
SU3-A
SU2-C
SU2-B
SU2-A
SU1-B
SU1-A
2877-2630 cal. BC
4241-4001 cal. BC
5000-4979 cal. BC
5520-5369 cal. BC
1D analyses
2D analyses
Energy of hydrological dynamics
Low
High
Gravel
Coarse sand
Medium sand
Fine sand
Clay-silt
Quartz %
Clay minerals %
Calcite %
Quartz %
Calcite %
Clay miner. %
Clay-silt
Fine sand
Medium sand
Coarse sand
Gravels and pebbles
Posidonia
Broken shells
Shells
Carbonate concretions
Sherds

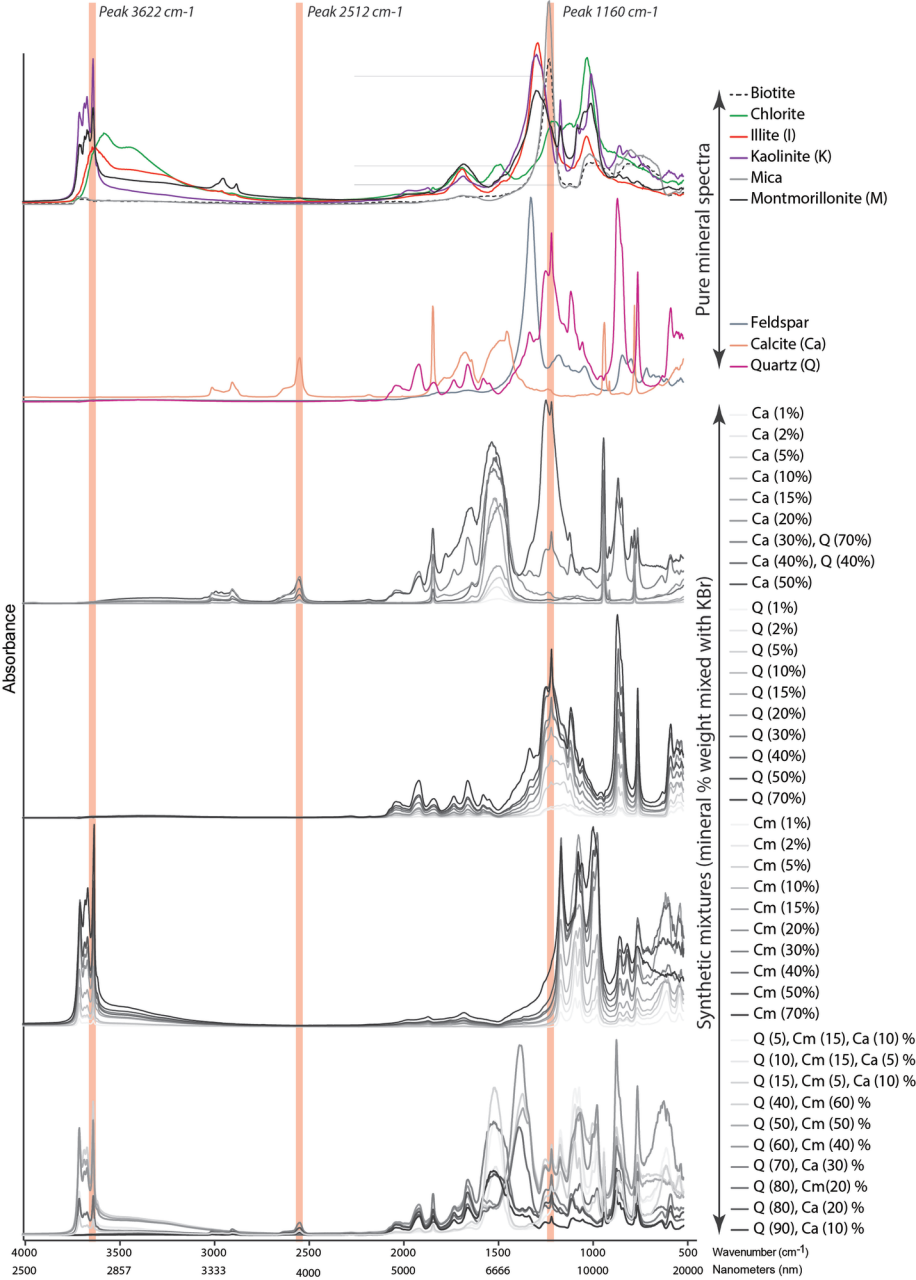
Peak 3622 cm-1
Peak 2512 cm-1
Peak 1160 cm-1
Biotite
Chlorite
Illite (I)
Kaolinite (K)
Mica
Montmorillonite (M)
Pure mineral spectra
Feldspar
Calcite (Ca)
Quartz (Q)
Absorbance
Ca (1%)
Ca (2%)
Ca (5%)
Ca (10%)
Ca (15%)
Ca (20%)
Ca (30%), Q (70%)
Ca (40%), Q (40%)
Ca (50%)
Q (1%)
Q (2%)
Q (5%)
Q (10%)
Q (15%)
Q (20%)
Q (30%)
Q (40%)
Q (50%)
Q (70%)
Cm (1%)
Cm (2%)
Cm (5%)
Cm (10%)
Cm (15%)
Cm (20%)
Cm (30%)
Cm (40%)
Cm (50%)
Cm (70%)
Q (5), Cm (15), Ca (10) %
Q (10), Cm (15), Ca (5) %
Q (15), Cm (5), Ca (10) %
Q (40), Cm (60) %
Q (50), Cm (50) %
Q (60), Cm (40) %
Q (70), Ca (30) %
Q (80), Cm(20) %
Q (80), Ca (20) %
Q (90), Ca (10) %
Synthetic mixtures (mineral % weight mixed with KBr)
4000
3500
3000
2500
2000
1500
1000
500
Wavenumber (cm-1)
2500
2857
3333
4000
5000
6666
10000
20000
Nanometers (nm)

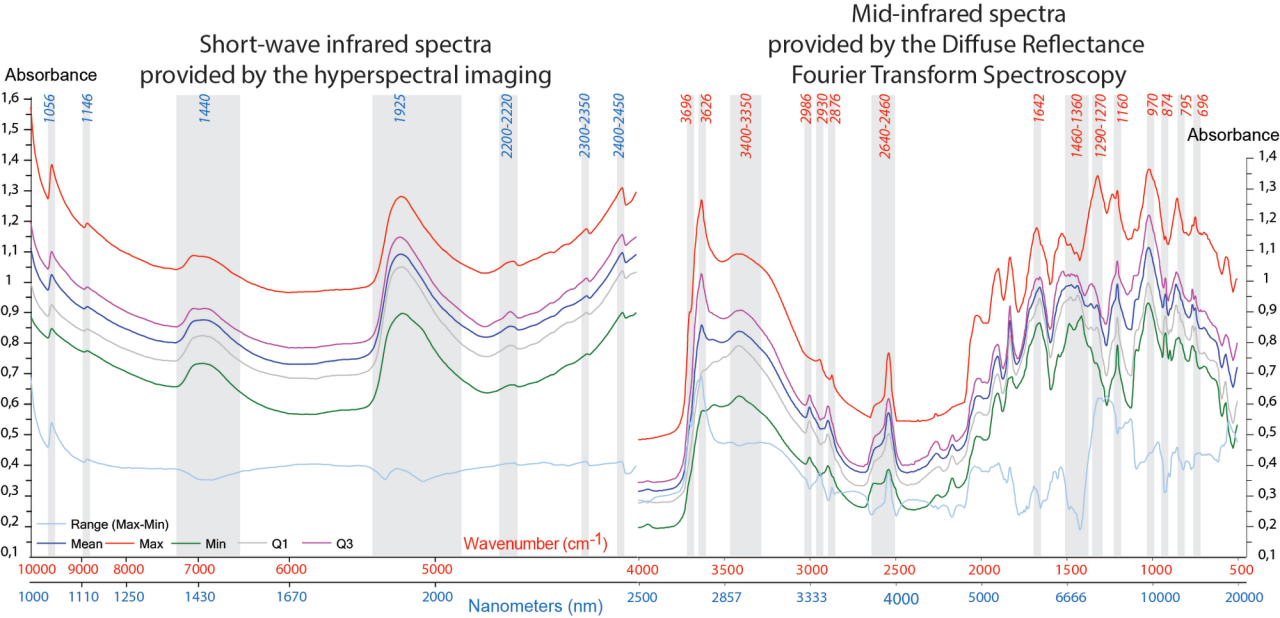
Short-wave infrared spectra
provided by the hyperspectral imaging
Mid-infrared spectra
provided by the Diffuse Reflectance
Fourier Transform Spectroscopy
Absorbance
Absorbance
1056
1146
1440
1925
2200-2220
2300-2350
2400-2450
3696
3626
3400-3350
2986
2930
2876
2640-2460
1642
1460-1360
1290-1270
1160
970
874
795
696
Range (Max-Min)
Mean
Max
Min
Q1
Q3
Wavenumber (cm-1)
Nanometers (nm)

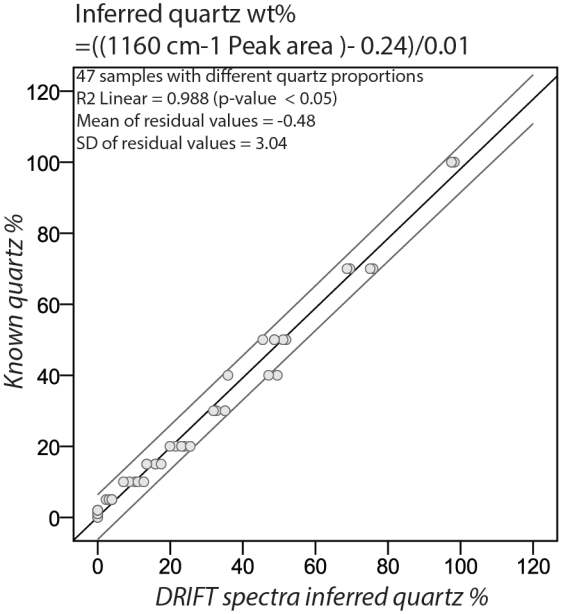
Inferred quartz wt%
=((1160 cm-1 Peak area)- 0.24)/0.01
47 samples with different quartz proportions
R2 Linear = 0.988 (p-value < 0.05)
Mean of residual values = -0.48
SD of residual values = 3.04
Known quartz %
DRIFT spectra inferred quartz %

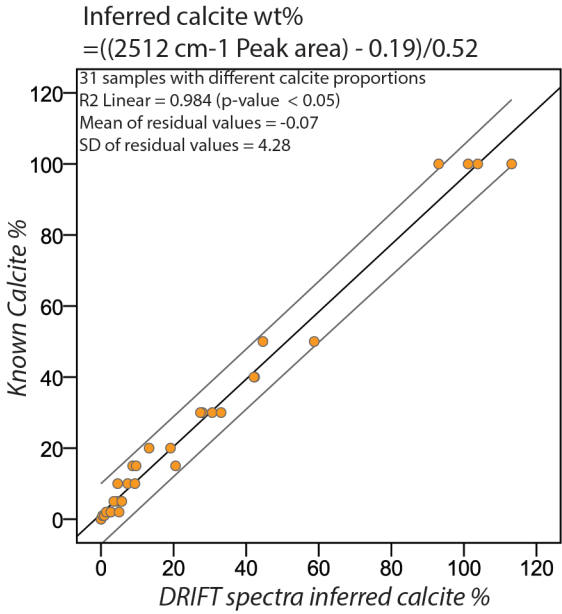
Inferred calcite wt%
=((2512 cm-1 Peak area) - 0.19)/0.52
31 samples with different calcite proportions
R2 Linear = 0.984 (p-value < 0.05)
Mean of residual values = -0.07
SD of residual values = 4.28
Known Calcite %
DRIFT spectra inferred calcite %

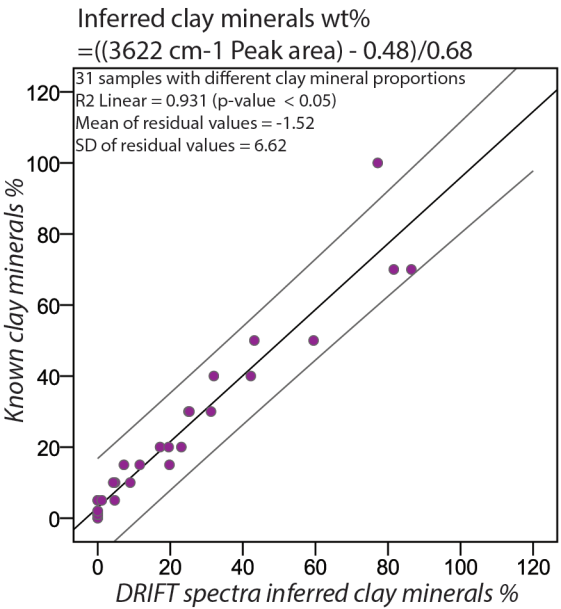
Inferred clay minerals wt%
=((3622 cm-1 Peak area) - 0.48)/0.68
31 samples with different clay mineral proportions
R2 Linear = 0.931 (p-value < 0.05)
Mean of residual values = -1.52
SD of residual values = 6.62
Known clay minerals %
DRIFT spectra inferred clay minerals %

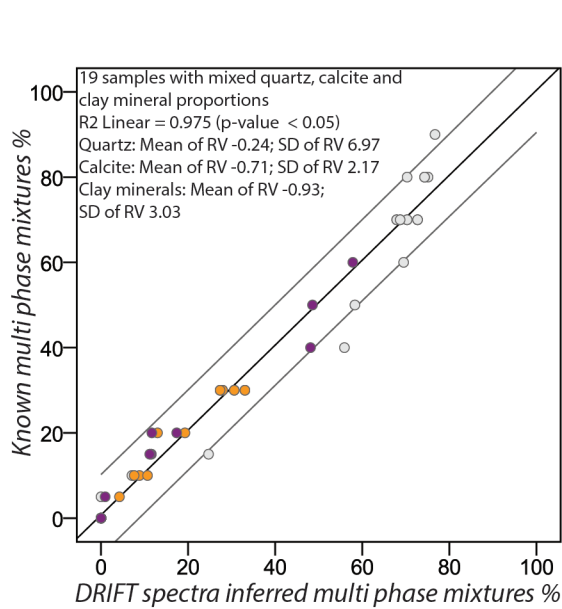
19 samples with mixed quartz, calcite and clay mineral proportions
R2 Linear = 0.975 (p-value < 0.05)
Quartz: Mean of RV -0.24; SD of RV 6.97
Calcite: Mean of RV -0.71; SD of RV 2.17
Clay minerals: Mean of RV -0.93;
SD of RV 3.03
Known multi phase mixtures %
DRIFT spectra inferred multi phase mixtures %

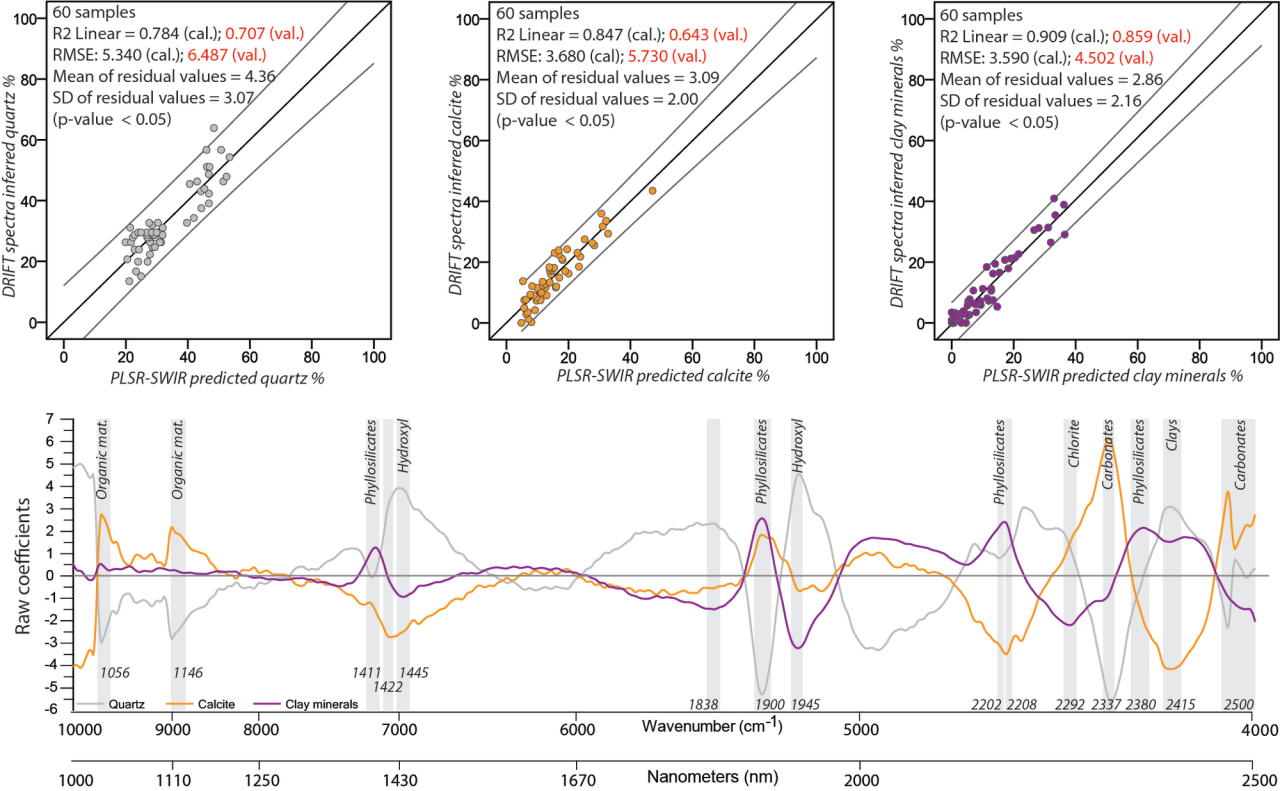
60 samples
R2 Linear = 0.784 (cal.); 0.707 (val.)
RMSE: 5.340 (cal.); 6.487 (val.)
Mean of residual values = 4.36
SD of residual values = 3.07
(p-value < 0.05)
DRIFT spectra inferred quartz %
PLSR-SWIR predicted quartz %
60 samples
R2 Linear = 0.847 (cal.); 0.643 (val.)
RMSE: 3.680 (cal); 5.730 (val.)
Mean of residual values = 3.09
SD of residual values = 2.00
(p-value < 0.05)
DRIFT spectra inferred calcite %
PLSR-SWIR predicted calcite %
60 samples
R2 Linear = 0.909 (cal.); 0.859 (val.)
RMSE: 3.590 (cal.); 4.502 (val.)
Mean of residual values = 2.86
SD of residual values = 2.16
(p-value < 0.05)
DRIFT spectra inferred clay minerals %
PLSR-SWIR predicted clay minerals %
Raw coefficients
Organic mat.
Organic mat.
Phyllosilicates
Hydroxyl
Phyllosilicates
Hydroxyl
Phyllosilicates
Chlorite
Carbonates
Phyllosilicates
Clays
Carbonates
1056
1146
1411
1422
1445
1838
1900
1945
2202
2208
2292
2337
2380
2415
2500
Quartz
Calcite
Clay minerals
Wavenumber (cm-1)
Nanometers (nm)

ID	Quartz wt%	Calcite wt%	KaolMontmIllite (1:1:1) wt%	KBr wt%
Ca1	0	1	0	99
Ca2	0	2	0	98
Ca5	0	5	0	95
Ca10	0	10	0	90
Ca15	0	15	0	85
Ca20	0	20	0	80
Ca50	0	50	0	50
Ca100	0	100	0	0
Cm1	0	0	1	99
Cm2	0	0	2	98
Cm5	0	0	5	95
Cm10	0	0	10	90
Cm15	0	0	15	85
Cm20	0	0	20	80
Cm30	0	0	30	70
Cm40	0	0	40	60
Cm50	0	0	50	50
Cm70	0	0	70	30
Cm100	0	0	100	0
Q1	1	0	0	99
Q2	2	0	0	98
Q5K15Ca10	5	10	15	70
Q5	5	0	0	95
Q10K15Ca5	10	5	15	70
Q10	10	0	0	90
Q15K5Ca10	15	10	5	70
Q15	15	0	0	85
Q20	20	0	0	80
Q20Cm80	20	0	80	0
Q30	30	0	0	70
Q40Cm60	40	0	60	0
Q40	40	0	0	60
Q40Ca40	40	40	0	20
Q50Cm50	50	0	50	0
Q50	50	0	0	50
Q60Cm40	60	0	40	0
Q70Ca30	70	30	0	0
Q70	70	0	0	30
Q80Cm20	80	0	20	0
Q80Ca20	80	20	0	0
Q90Ca10	90	10	0	0
Q100	100	0	0	0

Core	Depth (below soil topographic level)	Stratigraphic Units	Laboratory code	Dating support	14 C age in BP	Age calibrated (Reimer et al., 2020)
ALB-1	349 cm	SU2-C	Lyon-18795	Wood	4155 ± 30	2877 to 2630 BC
ALB-1	597 cm	SU2-C	Lyon-18796	Organic matter	5300 ± 30	4241 to 4001 BC
ALB-1	790-792 cm	SU2-B	Lyon-18797	Charcoal	6015 ± 35	5000 to 4797 BC
ALB-1	823-826 cm	SU2-A	Lyon-18798	Organic matter	6485 ± 35	5520 to 5369 BC

Correlations

DRIFTS inferred quartz (%)	1.00														
DRIFTS inferred calcite (%)	-0.36	1.00													
DRIFTS inferred clay-minerals (%)	-0.58	-0.39	1.00												
PLSR-SWIR predicted quartz (%)	**0.89**	-0.36	**-0.64**	1.00											
PLSR-SWIR predicted calcite (%)	-0.35	**0.92**	-0.37	-0.39	1.00										
PLSR-SWIR predicted clay-minerals (%)	**-0.60**	-0.35	**0.95**	**-0.68**	-0.39	1.00									
Clay-silt texture (%)	-0.56	-0.36	**0.91**	-0.58	-0.37	**0.86**	1.00								
Fine-Sand (%)	0.52	-0.13	-0.52	**0.62**	-0.10	-0.56	**-0.62**	1.00							
Medium-Sand (%)	0.48	0.39	**-0.78**	0.46	0.40	**-0.75**	**-0.74**	0.23	1.00						
Coarse-Sand (%)	-0.16	0.39	-0.18	-0.21	0.37	-0.06	-0.25	-0.37	0.01	1.00					
Total sand (%)	0.57	0.32	**-0.90**	**0.60**	0.34	**-0.86**	**-0.99**	**0.65**	**0.74**	0.23	1.00				
Gravel (%)	0.00	0.27	-0.13	-0.07	0.25	-0.12	-0.15	-0.16	0.06	0.16	0.01	1.00			
Magnetic susceptibility	-0.25	0.37	-0.02	-0.22	0.45	-0.11	-0.03	0.04	0.08	-0.08	0.02	0.09	1.00		
Moisture peak at 1935 nm	0.09	0.13	-0.04	0.06	0.17	-0.10	-0.06	-0.06	0.30	-0.25	0.03	0.24	0.23	1.00	
Hydroxyl bonds peak at 1450 nm	-0.41	-0.18	**0.69**	-0.47	-0.17	**0.68**	**0.73**	**-0.61**	-0.37	-0.20	**-0.74**	-0.01	0.03	0.44	1.00